

Abort Performance for a Winged-Body Single-Stage to Orbit Vehicle

Jeffery A. Lyon
The George Washington University
Joint Institute for Advancement of Flight Sciences
Langley Research Center • Hampton, Virginia

Abstract

Optimal control theory is employed to determine the performance of abort to orbit (ATO) and return to launch site (RTLS) maneuvers for a single-stage to orbit vehicle. The vehicle configuration examined is a seven engine, winged-body vehicle, that lifts-off vertically lands horizontally. The abort maneuvers occur as the vehicle ascends to orbit and are initiated when the vehicle suffers an engine failure. The optimal control problems are numerically solved in discretized form via a non-linear programming (NLP) algorithm. A description highlighting the attributes of this NLP method is provided.

ATO maneuver results show that the vehicle is capable of ascending to orbit with a single engine failure at lift-off. Two engine out ATO maneuvers are not possible from the launch pad, but are possible after launch when the thrust to weight ratio becomes sufficiently large. Results show that single engine out RTLS maneuvers can be made for up to 180 seconds after lift-off and that there are scenarios for which RTLS maneuvers should be performed instead of ATO maneuvers.

Contents

Abstract	iii
Table of Contents	v
List of Tables	vii
List of Figures	viii
Nomenclature	x
1 Introduction	1
2 SSTO Background	3
3 SSTO Model Description	6
3.1 Equations of Motion	6
3.2 Gravity Model	7
3.3 Atmosphere Model	7
3.4 Aerodynamics	8
3.5 Propulsion	13
4 Solution Method	14
4.1 Optimal Control	14
4.1.1 Single Phase Optimal Control Problem	14
4.1.2 Multiple Phase Optimal Control Problem	16
4.2 Numerical Approach	18

4.3	Algorithm Performance	22
5	Abort Maneuvers	25
5.1	Baseline Performance Problem Description	25
5.2	Baseline Performance Results	27
5.3	ATO Maneuver Problem Descriptions	35
5.4	ATO Maneuver Results	36
5.5	RTLS Maneuver Problem Descriptions	43
5.5.1	Maximize Time of Abort	44
5.5.2	Payload Returned To Launch Site	45
5.6	RTLS Maneuver Results	47
6	Summary	56
A	Development of 3-DOF Equations of Motion for a SSTO Vehicle	60
A.1	Reference Frames	60
A.1.1	Earth-Centered Inertial Frame	60
A.1.2	Earth-Centered Rotating Frame	61
A.1.3	Position Frame	61
A.1.4	Velocity Frame	62
A.1.5	Body Frame	62
A.2	Development of Equations of Motion	63
B	NLP Scheme Used To Solve Optimal Control Problems	68

List of Tables

2.1	Miscellaneous Vehicle Parameters	5
3.1	Atmospheric Parameters	8
3.2	Coefficients Used in Aerodynamic Models	13
4.1	Numerical Approach Results	24

List of Figures

2.1	Winged-Body Configuration	4
3.1	Comparison of Model and Tabular Lift Coefficients	10
3.2	Comparison of Model and Tabular Drag Coefficients	10
3.3	Comparison of Model and Tabular Lift Coefficients	11
3.4	Comparison of Model and Tabular Drag Coefficients	12
4.1	Multiple Phase Time-line	17
4.2	Ground-track Comparison	24
5.1	Baseline Ascent Trajectory : Air Speed	28
5.2	Baseline Ascent Trajectory : Relative Flight-Path	28
5.3	Baseline Ascent Trajectory : Altitude	29
5.4	Baseline Ascent Trajectory : Mass	29
5.5	Baseline Ascent Trajectory : Relative Heading	30
5.6	Baseline Ascent Trajectory : Groundtrack	30
5.7	Baseline Ascent Trajectory : Throttle	31
5.8	Baseline Ascent Trajectory : Attack Angle	32
5.9	Baseline Ascent Trajectory : Bank Angle	32
5.10	Active Inequality Constraints in Baseline Ascent	33
5.11	Minimizing Attack Angle in Transonic Region	34
5.12	Baseline Ascent Trajectory : Drag Profile	34
5.13	ATO Maneuver Performance	38

5.14 Drag Profiles for ATO Maneuvers Initiated at 50 and 60 Seconds After Launch	39
5.15 Lofting of ATO Maneuvers Initiated 60 Seconds After Launch	40
5.16 Attack Angle Profiles for ATO Maneuvers Initiated 60 Seconds After Launch	41
5.17 Mass Profiles for ATO Maneuvers Initiated 60 Seconds After Launch	41
5.18 Throttle Profiles for ATO Maneuvers Initiated 60 Seconds After Launch	42
5.19 RTLS Phases	43
5.20 RTLS Maximum Abort Time Versus Maximum Attack Angle For Single Engine Out Scenario	47
5.21 RTLS Max. Alpha = 90, Altitude vs Air Speed	48
5.22 RTLS Max. Alpha = 90, Attack Angle vs Time After Launch	49
5.23 RTLS Max. Alpha = 90, Groundtrack	49
5.24 RTLS Max. Alpha = 90, Thrust Profile	50
5.25 RTLS Max. Alpha = 90, Heading Angle History	51
5.26 Maximum Abort Time RTLS Maneuvers : Relative Velocity Profile .	52
5.27 Maximum Abort Time RTLS Maneuvers : Altitude Profile	52
5.28 Maximum Abort Time RTLS Maneuvers : Ground-track	53
5.29 Maximum Abort Time RTLS Maneuvers : Attack Angle Profile . . .	54
5.30 Maximum Abort Time RTLS Maneuvers : Throttle Profile	55
A.1 I-frame and R-frame	61
A.2 R-frame and P-frame	62
A.3 P-frame and S-frame	63
A.4 S-frame and B-frame	64
B.1 NLP Scheme	69

Nomenclature

Roman Symbols

a	Speed of Sound, ft/s
A_e	Exit Area of SSME Derivative Engine, ft ²
c_D	Drag Coefficient
c_L	Lift Coefficient
C	State/Control Inequality Constraints
g	Acceleration Due to Gravity, ft/s ²
g_0	Acceleration of Gravity at Sea Level, ft/s ²
D	Drag, lbf
I_{sp}	Specific Impulse, s
\mathcal{J}	Objective Function
k	Ratio of Specific Heats
L	Lift, lbs
m	SSTO Vehicle Mass, slugs
M	Mach Number
$N_{engines}$	Number of SSME Derivative Engines
p	Atmospheric Pressure, lbs/ft ²
p_0	Atmospheric Pressure at Sea Level, lbs/ft ²
q	Dynamic Pressure, lbs/ft ²
\mathcal{P}	Free Parameter Inequality Constraints
r	Radial Distance from the Center of the Earth to vehicle center of mass, ft

r_E	Radius of Earth, ft
R_{gas}	Gas Constant for Air
S	Reference Area, ft ²
S	State-Only Inequality Constraints
T	Thrust, lbs
T_{vac}	Vacuum Thrust of SSME Derivatives Engine, lbs
T	Temperature, °R
v	Airspeed, ft/s

Greek Symbols

α	Attack-Angle, rad
β_p	Atmospheric Pressure Scale Height, ft
β_r	Atmospheric Density Scale Height, ft
ϕ	Latitude, rad
Φ	Phase of Multiple Phase Optimal Control Problem
γ	Flight-Path Angle, rad
η	SSME Derivative Engine Throttle
μ	Bank Angle, rad
θ	Longitude, rad
ρ	Atmospheric Density, slugs/ft ³
ρ_0	Atmospheric Pressure at Sea Level, slugs/ft ³
ω	Angular Velocity of the Earth, rad/s
ψ	Heading Angle, rad
Ψ	Boundary Conditions

Subscripts

0	Initial Value
f	Final Value
TAB	Tabular Aerodynamic Coefficient

Acronyms

ATO	Abort To Orbit
DOF	Degree Of Freedom
JIAFS	Joint Institute for the Advancement of Flight Sciences
LH	Liquid Hydrogen
LOX	Liquid Oxygen
NASA	National Aeronautics and Space Administration
NLP	Non-Linear Programming
RTLS	Return To Launch Site
SSME	Space Shuttle Main Engine
SSTO	Single Stage To Orbit

Chapter 1

Introduction

In 1993, Congress asked the National Aeronautics and Space Administration (NASA) to address the future needs of U.S. space transportation systems. Although current systems meet the functional needs of the U.S. space program, the systems lack cost effectiveness, reliability and operability. As a result, the ability of U.S. industry to compete in the international launch market has suffered.

In response to the Congressional request, NASA studied [1] possible architectures for the next generation of launch vehicles. This next generation of vehicles is to address the deficiencies of the current systems and at the same time focus on increasing safety. Recognizing the major advances in technology and vehicle design that have been made within the past decade, the NASA recommended the development of a fully reusable single-stage to orbit (SSTO) vehicle.

Addressing the issue of increased safety, the purpose of this work is to determine the abort performance of abort to orbit (ATO) and return to launch site (RTLS) maneuvers for a SSTO vehicle. The vehicle configuration considered is a seven engine, winged-body vehicle that lifts-off vertically and lands horizontally. The abort maneuvers occur as the vehicle ascends to orbit and are initiated when the SSTO vehicle suffers an engine failure. A point mass model is used to describe the motion of the SSTO vehicle. A non-linear programming (NLP) method is developed for solving optimal control problems is used in the analysis.

Before the abort maneuvers are studied, a baseline ascent trajectory is generated.

In this ascent the vehicle has a full complement of engines. The trajectory is shaped so as to maximize the amount of mass delivered to orbit. This trajectory provides a reference to which the abort maneuvers can be compared.

The amount of mass delivered to orbit is also used as a performance measure for the ATO maneuvers. The performance for problems with various engine failure times is obtained. The vehicle travels on the baseline ascent trajectory until the time of engine failure. Single-engine and two-engine-out scenarios are examined.

Several problems are investigated for the RTLS maneuvers. Like the ATO maneuvers, the vehicle initially travels on the baseline ascent trajectory before suffering an engine failure. The maximum time after launch that the vehicle can perform an RTLS maneuver is determined. Also, the limits on the payload mass that can be returned to the launch site are determined for specified engine failure times.

Previously [2], abort capabilities for a similar vehicle were determined. In this study, the maximum allowable normal force and terminal altitude for the RTLS maneuvers are significantly larger than those allowed for this study.

The results of computations for a winged-body SSTO configuration are given in this paper. Also, the attributes of the NLP method are described.

Chapter 2

SSTO Background

A single-stage launch vehicle discards only propellants while ascending to orbit. For a single-stage vehicle, each pound of structure trades off for a pound of payload; therefore minimizing the dry weight of the vehicle is crucial in the design process. Because technologies required to produce adequate performance margins have been lacking, the feasibility of a single-stage launch vehicle has been questioned.

In contrast, a multiple-stage launch vehicle discards both propellants and structural weight while ascending to orbit. By staging, the weight and performance required by each stage is reduced, thus making the multiple-stage launch vehicle a feasible alternative. However, staging also introduces undesirable operational complexities and cost.

Recent technological advances in the fields of material science and propulsion have influenced NASA to propose the development of a single-stage launch vehicle. One of the proposed designs is a winged-body configuration.

The selection and design of this configuration is described in [3]. As illustrated in Figure 2.1, this vehicle is powered by seven space shuttle main engine (SSME) derivative engines. This vehicle launches vertically, and lands horizontally. The vehicle uses chemical propulsion with liquid hydrogen (LH) and liquid oxygen (LOX) serving as the fuel and oxidizer respectively. As shown in Figure 2.1, the payload bay separates the forward LOX and aft LH tanks. In table 2.1 various vehicle parameters are given including the performance characteristics of the SSME derivative engines.

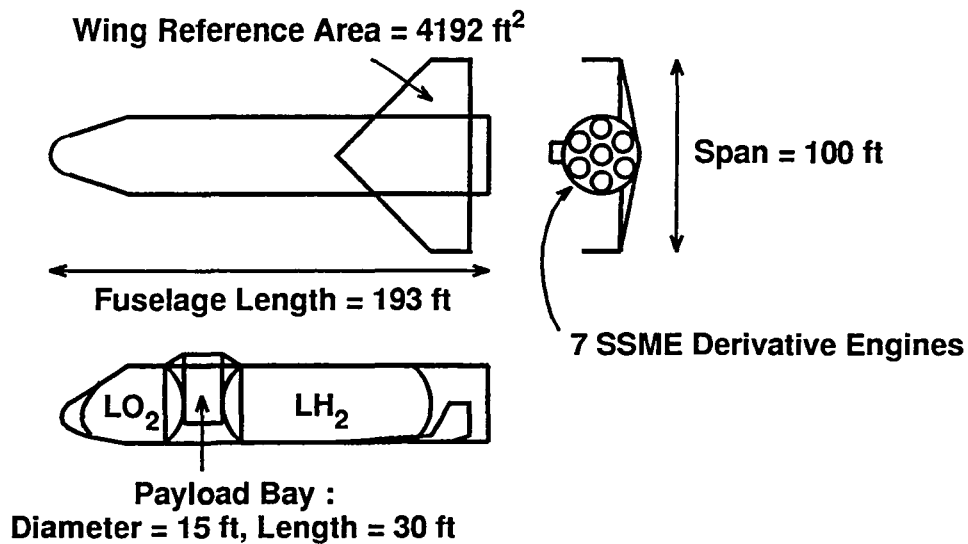


Figure 2.1: Winged-Body Configuration

Issues that must be addressed in order for the SSTO vehicle to demonstrate improved operability are treated in [4]. This document discusses lessons that have been learned from the space shuttle program and other launch vehicle concepts.

In [5] requirements for the SSTO vehicle are outlined. This study addresses the requirement that the vehicle is to have “At minimum, single-engine-out capability throughout ascent (either return to site or abort to orbit/once around)”.

Table 2.1: Miscellaneous Vehicle Parameters

Number of Engines	7	
Vacuum Thrust	463.90	klbf
Vacuum Specific Impulse	447.3	sec
Engine Mass	6.79	klbm
Oxider To Fuel Ratio	6.0	
Exit Area	27.55	ft ²
Vehicle Dry Mass	206.50	klbm
Vehicle Gross Mass at Lift-Off	2383.43	klbm
Nominal Payload Mass	20.0	klbm
Vehicle Reference Area	4192.2	ft ²

Chapter 3

SSTO Model Description

In this section, the physical model used for the abort maneuvers is discussed. Equations describing the motion of the vehicle, the acceleration due to gravity, the atmosphere, the aerodynamics and the propulsion are given.

3.1 Equations of Motion

The center of mass motion for a thrusting SSTO vehicle flying over a rotating Earth can be described by (see appendix A for development)

$$\left. \begin{aligned} \dot{\theta} &= v \cos \gamma \cos \psi / (r \cos \phi) \\ \dot{\phi} &= v \cos \gamma \sin \psi / r \\ \dot{h} &= v \sin \gamma \\ \dot{v} &= (T \cos \alpha - D) / m - g \sin \gamma + \omega^2 r \cos \phi (\sin \gamma \cos \phi - \cos \gamma \sin \phi \sin \psi) \\ \dot{\psi} &= (T \sin \alpha + L) \sin \mu / (m v \cos \gamma) - \omega^2 r \sin \phi \cos \phi \cos \psi / (v \cos \gamma) \\ &\quad + 2\omega (\tan \gamma \cos \phi \sin \psi - \sin \phi) / (v \cos \gamma) - (v/r) \cos \gamma \cos \psi \tan \phi \\ \dot{\gamma} &= (T \sin \alpha + L) \cos \mu / (m v) + (\omega^2 r / v) \cos \phi (\cos \gamma \cos \phi + \sin \gamma \sin \phi \sin \psi) \\ &\quad + 2\omega \cos \phi \cos \psi + (v/r - g/v) \cos \gamma \\ \dot{m} &= -N_{engines} \eta T_{vac} / (g_0 I_{sp}) \end{aligned} \right\} \quad (3.1)$$

The state variables for this system of equations are longitude θ , latitude ϕ , altitude

h , airspeed v , relative heading ψ , relative flight-path γ and mass m . The controls are attack angle α , bank angle μ and throttle η . These equations assume that moment equilibrium can be maintained by the control system. These equations also assume that a positive bank angle generates a heading to the north for a vehicle flying west to east.

3.2 Gravity Model

The Earth is assumed to be a sphere whose radius r_E represents mean sea level. If r is the radial distance from the center of the Earth to the center of gravity of the vehicle, the acceleration of gravity is given by the inverse square law

$$g = g_0(r_E/r)^2 \quad (3.2)$$

3.3 Atmosphere Model

A simple exponential model was adopted for the atmosphere model. In this model the atmospheric pressure is calculated by

$$p = p_0 e^{-(h/\beta_p)} \quad (3.3)$$

Similarly, the atmospheric density is found with

$$\rho = \rho_0 e^{-(h/\beta_r)} \quad (3.4)$$

Assuming that air behaves as an ideal gas, the temperature is calculated using

$$T = p/(\rho R_{gas}) \quad (3.5)$$

Table 3.1: Atmospheric Parameters

r_E	2.0925721e+07	ft
p_0	2.1162e+03	psf
β_p	2.3127e+04	ft
ρ_0	2.3769e-03	slugs/ft ³
β_r	2.3341e+04	ft
R_{gas}	1.7163e+03	ft ² /sec ² °R
k	1.4	

Since air is assumed to behave as an ideal gas, the speed of sound may be calculated with

$$\left. \begin{aligned} a &= \sqrt{kR_{gas}\mathcal{T}} \\ &= \sqrt{kp/\rho} \end{aligned} \right\} \quad (3.6)$$

Table 3.1 summarizes the values of the constants used to evaluate atmospheric quantities.

3.4 Aerodynamics

The lift and drag acting on the SSTO vehicle are related to the lift and drag coefficients (c_L and c_D) as follows

$$L = \frac{1}{2}\rho v^2 S c_L \quad (3.7)$$

$$D = \frac{1}{2}\rho v^2 S c_D \quad (3.8)$$

where S is the aerodynamic reference area. The lift and drag coefficients are functions of mach number and angle of attack. Mach number is found with

$$M = \frac{v}{a} \quad (3.9)$$

The aerodynamic coefficients are modeled with

$$c_L(M, \alpha) = c_{L\alpha}(M) \alpha \quad (3.10)$$

$$c_D(M, \alpha) = c_{D_o}(M) + c_{D\alpha}(M) \alpha^2 \quad (3.11)$$

In this model, the coefficients $c_{L\alpha}$ and $c_{D\alpha}$ are chosen so as to minimize the Euclidean norm of the error between the model and existing tabular data for the lift and drag coefficients at the table values. The Euclidean norm of the error between the lift model and the lift coefficient data (c_{LTAB}) is described by

$$\mathcal{J}_L = \sum_j \frac{1}{2} [c_{L\alpha} \alpha_j - c_{LTAB}(\alpha_j)]^2 \quad -\frac{\pi}{2} \leq \alpha_j \leq \frac{\pi}{2} \quad (3.12)$$

Note that only the tabular lift coefficients corresponding to attack angles in the interval $[-\pi/2, \pi/2]$ influence \mathcal{J}_L . The value of $c_{L\alpha}$ that minimizes \mathcal{J}_L is

$$c_{L\alpha} = \frac{\sum_j \alpha_j c_{LTAB}(\alpha_j)}{\sum_j \alpha_j^2} \quad -\frac{\pi}{2} \leq \alpha_j \leq \frac{\pi}{2} \quad (3.13)$$

Similarly, the Euclidean norm of the error between the drag model and the drag coefficient data (c_{DTAB}) is described by function

$$\mathcal{J}_D = \sum_j \frac{1}{2} [c_{D_o} + c_{D\alpha} \alpha_j^2 - c_{DTAB}(\alpha_j)]^2 \quad -\frac{\pi}{2} \leq \alpha_j \leq \frac{\pi}{2} \quad (3.14)$$

where, for simplicity, the coefficient c_{D_o} was chosen to be the value of the tabular drag coefficient for zero angle of attack. The value of $c_{D\alpha}$ that minimizes \mathcal{J}_D is

$$c_{D\alpha} = \frac{\sum_j [c_{DTAB}(\alpha_j) - c_{D_o}] \alpha_j^2}{\sum_j \alpha_j^4} \quad -\frac{\pi}{2} \leq \alpha_j \leq \frac{\pi}{2} \quad (3.15)$$

Figures 3.1 through 3.4 illustrate the performance of the aerodynamic models in comparison to the tabular data. Surface plots of the aerodynamic models for the lift and drag coefficients are provided in Figures 3.1 and 3.2. In these figures the tabular data points are included as asterisks to provide an idea of how accurately the models approximate the tabular data. The shapes of these surfaces in the transonic region make modeling the surfaces with a simple analytic expression difficult.

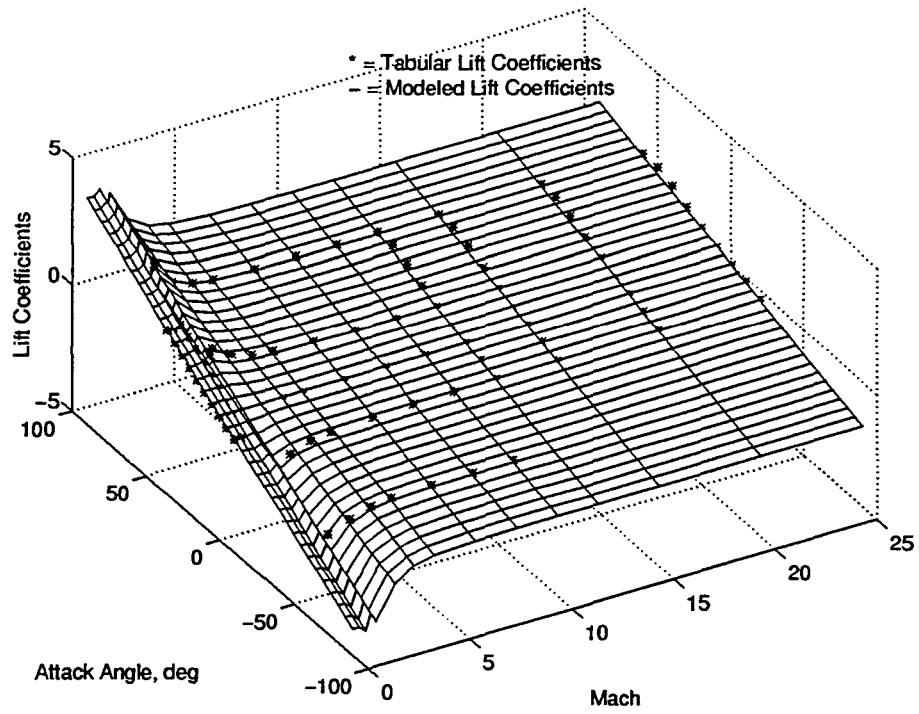


Figure 3.1: Comparison of Model and Tabular Lift Coefficients

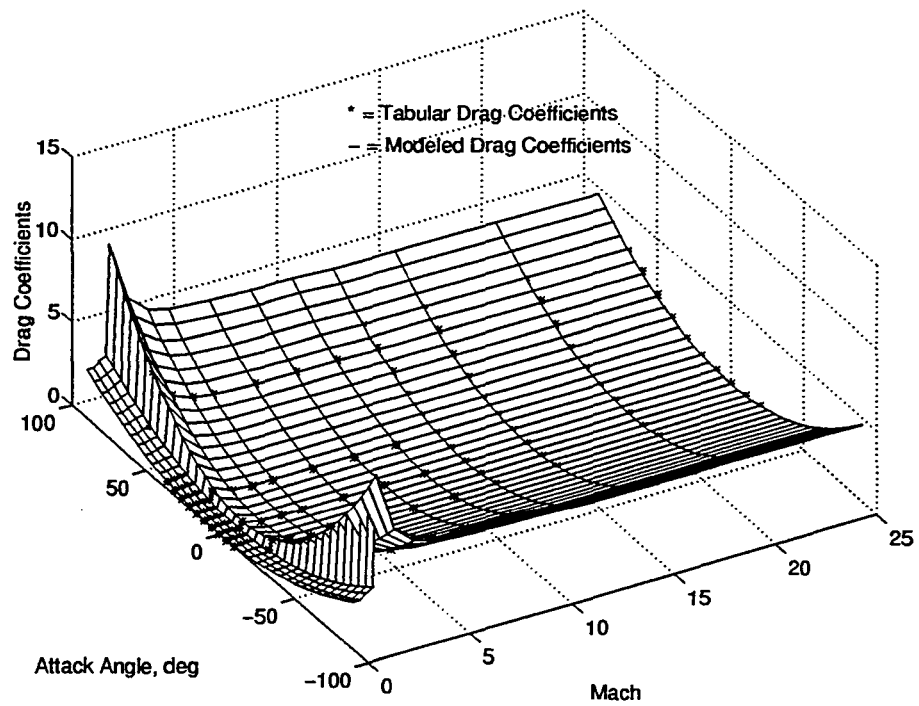


Figure 3.2: Comparison of Model and Tabular Drag Coefficients

Defining the error in the aerodynamic models as the difference between the modeled coefficients and the tabular coefficients, Figures 3.3 and 3.4 illustrate the absolute error in the aerodynamic models for the lift and drag coefficients respectively. The tabular data consists of three different subtables corresponding to subsonic, supersonic, and hypersonic mach ranges. Each of the subtables are defined with different attack angles. Because the tabular data consists of three subtables, three different surfaces are required to describe the absolute error. These figures show that the aerodynamic models adequately approximate the tabular data.

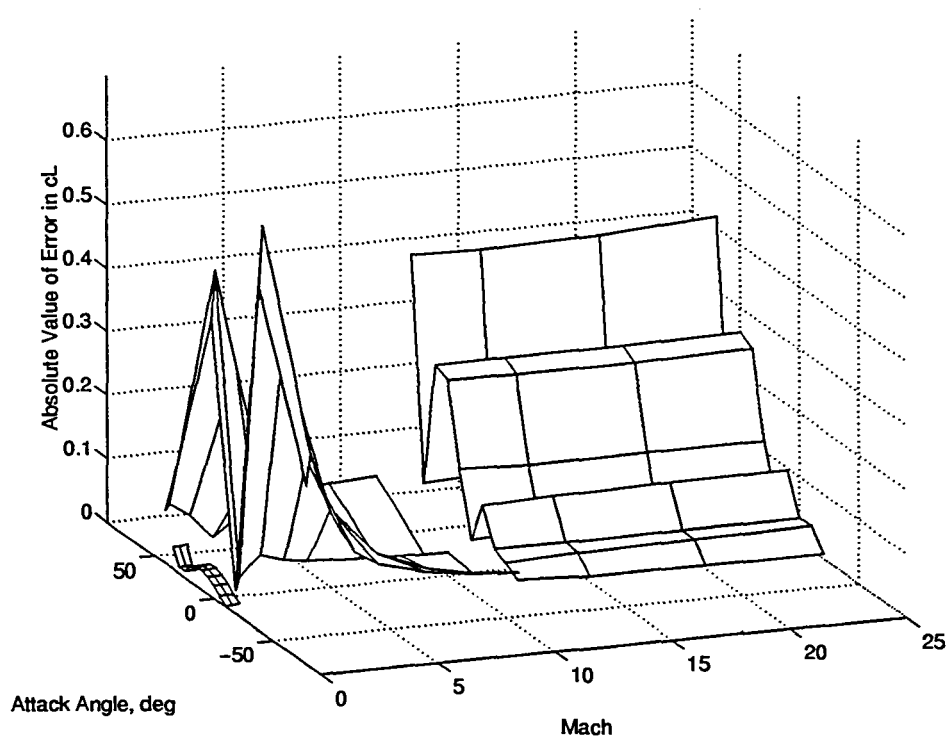


Figure 3.3: Comparison of Model and Tabular Lift Coefficients

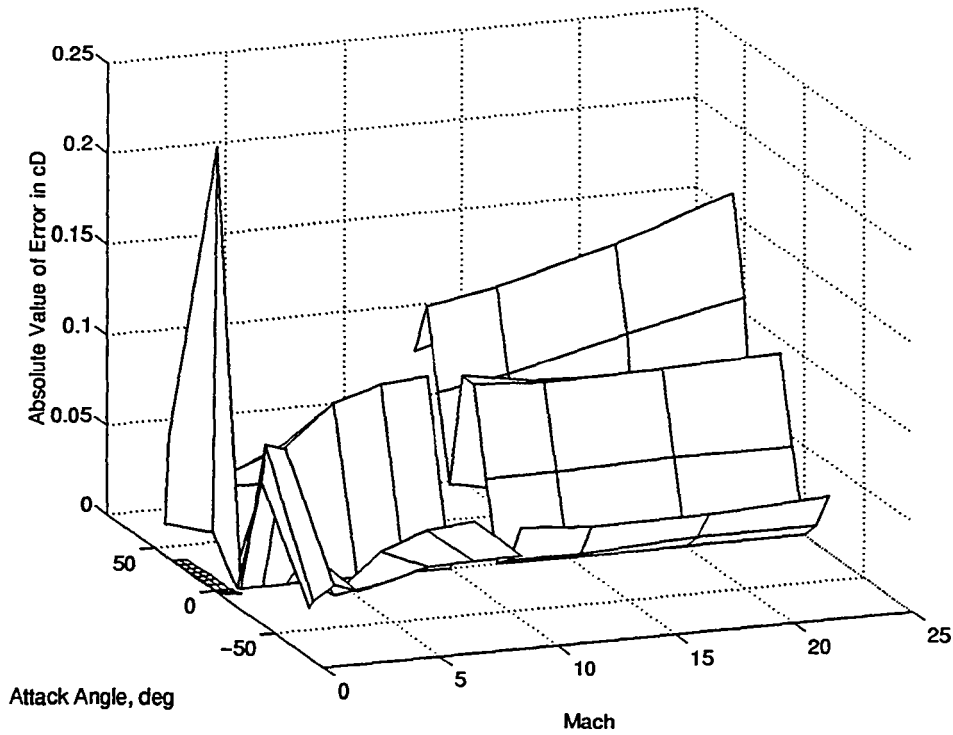


Figure 3.4: Comparison of Model and Tabular Drag Coefficients

Values for $c_{L\alpha}$, c_{D_0} and $c_{D\alpha}$ are defined for various mach numbers in table 3.2. Interpolation is used to determine the values of these coefficients for mach numbers not represented in the table. The interpolation technique used to evaluate these coefficients is an alternative method to piecewise linear interpolation.

Many optimization schemes, including the one employed in this study, require derivative information. In general, piecewise linear interpolation does not provide first derivative continuity. For this reason, optimization schemes that use piecewise linear interpolation may fail. The technique used in this analysis guarantees second derivative continuity. A detailed description of this interpolation technique is given in [6]

Table 3.2: Coefficients Used in Aerodynamic Models

Mach	$c_{L\alpha}$	c_{D_o}	$c_{D\alpha}$
0.0000	2.5004	0.0277	1.1678
0.3000	2.5004	0.0277	1.1678
0.6000	2.6467	0.0388	1.2819
0.9500	2.0782	0.0204	1.3840
1.1000	2.4824	0.4071	3.9257
2.0000	1.6739	0.0918	2.6077
3.0000	1.3597	0.0811	2.1939
4.0000	1.2436	0.0767	2.0492
6.0000	1.1742	0.0727	1.9773
8.0000	1.1465	0.0710	1.9499
10.0000	1.1335	0.0709	1.9389
12.0000	1.1497	0.0720	1.8792
15.0000	1.1402	0.0704	1.8711
20.0000	1.1285	0.0710	1.8550
25.0000	1.1208	0.0739	1.8314

3.5 Propulsion

This SSTO vehicle model has seven Space Shuttle Main Engine (SSME) derivative engines. The total thrust of the SSTO vehicle is given by

$$T = N_{engines}(\eta T_{vac} - A_{ep}) \quad (3.16)$$

and pertinent engine parameters are found in table 2.1.

Chapter 4

Solution Method

This section begins by discussing optimal control at a generic level. Single phase and multiple phase optimal control problems are described. Next, a numerical approach for transforming the optimal control problems into algebraic non-linear programming (NLP) problems is outlined. Finally, the performance of the algorithm is illustrated by solving a simple example problem.

4.1 Optimal Control

The objective of optimal control theory is to determine the control signals that will cause a system to satisfy the physical constraints and at the same time minimize some performance criterion.

4.1.1 Single Phase Optimal Control Problem

For a specified initial time t_0 , choose the initial states $x(t_0) \in \mathcal{R}^n$, final time t_f , control history $[u(\tau) \in \mathcal{R}^m \ t_0 \leq \tau \leq t_f]$ and free parameters $z \in \mathcal{R}^j$ to minimize the scalar objective function

$$\mathcal{J} = \mathcal{J}[x(t_0), x(t_f), t_f, z] \tag{4.1}$$

The objective function or performance index is subject to the dynamical constraints

$$x(t) - \left(x(t_0) + \int_{t_0}^t f[x(\tau), u(\tau), z] d\tau \right) = 0 \quad (4.2)$$

and boundary conditions specified as

$$\Psi[x(t_0), x(t_f), t_f, z] = 0 \quad (4.3)$$

The control function $u(\tau)$ is assumed to be integrable on the interval $t_0 \leq \tau \leq t_f$.

Inequality constraints may also exist. These constraints appear in either of two forms:

state/control

$$\mathcal{C}(x, u, t, z) \leq 0 \quad (4.4)$$

or state-only

$$\mathcal{S}(x, t, z) \leq 0 \quad (4.5)$$

The constraints are categorized in this manner because the control of $\mathcal{S}(x, t, z)$ is obtained only by changing the q th time derivative of the constraint $\mathcal{S}^q(x, t, z)$ which depends explicitly on the controls u . As the state trajectory enters the constraint boundary $\mathcal{S}(x, t, z) = 0$, the tangency constraints

$$\begin{bmatrix} \mathcal{S}(x, t, z) = 0 \\ \mathcal{S}^1(x, t, z) = 0 \\ \vdots \\ \mathcal{S}^{q-1}(x, t, z) = 0 \end{bmatrix} \quad (4.6)$$

must be satisfied. These tangency constraints apply for state trajectories leaving the constraint boundary as well. Since the control appears explicitly in 4.4, "tangency" is not required for these inequality constraints [7]. As a result satisfying state/control

inequality constraints is typically somewhat easier than satisfying state-only inequality constraints.

A useful example of a free parameter z is the duration of the trajectory in a free time problem. The state equations for a free time problem

$$\frac{dx}{dt} = f(x, u, t) \quad t_0 \leq t \leq t_f \quad t_0 \text{ fixed and } t_f \text{ free} \quad (4.7)$$

can be recast as

$$\frac{dx}{d\tau} = (t_f - t_0)f(x, u, \tau) \quad 0 \leq \tau \leq 1 \quad (4.8)$$

where

$$\tau = (t - t_0)/(t_f - t_0) \quad (4.9)$$

One technique for solving a free time problem is to select a free parameter to represent the duration of the trajectory $t_f - t_0$. An additional inequality constraint

$$t_f - t_0 \geq 0 \quad (4.10)$$

prevents negative time scaling of the state equations thus ensuring that time monotonically increases.

4.1.2 Multiple Phase Optimal-Control Problem

Single phase optimal control problems may only have boundary conditions at the initial and final times of the trajectory. Frequently, a need arises for additional boundary conditions in the interior of the interval $[t_0, t_f]$.

Multiple phase optimal control problems allow for the existence of interior boundary conditions. The states and controls of each phase of a multiple phase problem can be represented by

$$\left. \begin{array}{l} x_k \quad k = 1, \dots, L \quad x_k \in \mathcal{R}^{n_k} \\ u_k \quad k = 1, \dots, L \quad u_k \in \mathcal{R}^{m_k} \end{array} \right\} \quad (4.11)$$

where L is the total number of phases. If the initial and final times of each phase are denoted by t_{k0} and t_{kf} respectively, the initial and final values of the states of each phase are

$$\left. \begin{aligned} x_{k0} &= x_k(t_{k0}) & k &= 1, \dots, L \\ x_{kf} &= x_k(t_{kf}) & k &= 1, \dots, L \end{aligned} \right\} \quad (4.12)$$

Figure 4.1 shows a time-line for a multiple phase problem. In this figure, the phases are denoted by Φ_k .

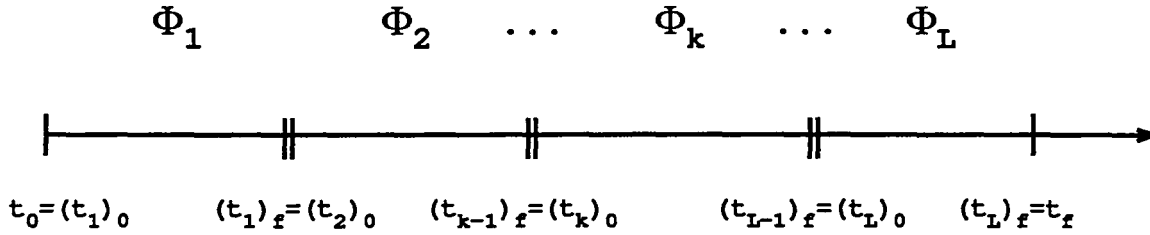


Figure 4.1: Multiple Phase Time-line

The objective function for a multiple phase problem is of the form

$$\mathcal{J} = \mathcal{J}[x_{10}, x_{1f}, x_{20}, x_{2f}, \dots, x_{L0}, x_{Lf}, z] \quad (4.13)$$

The multiple phase dynamical constraints are

$$x_k(t) - \left(x_k(t_{k0}) + \int_{t_{k0}}^t f[x_k(\tau), u_k(\tau), z] d\tau \right) = 0 \quad k = 1, \dots, L \quad (4.14)$$

with the boundary conditions

$$\Psi[x_{10}, x_{1f}, x_{20}, x_{2f}, \dots, x_{L0}, x_{Lf}, z] = 0 \quad (4.15)$$

The inequality constraints are expressed as

$$\mathcal{C}(x_k, u_k, t, z) \leq 0 \quad k = 1, \dots, L \quad (4.16)$$

and

$$\mathcal{S}(x_k, t, z) \leq 0 \quad k = 1, \dots, L \quad (4.17)$$

4.2 Numerical Approach

In this approach, optimal control problems are transformed into algebraic NLP problems of the form

$$\left. \begin{array}{l} \text{minimize} \quad \mathcal{J}(y) \\ y \in \mathcal{R}^M \\ \text{subject to :} \\ \quad \quad \quad E(y) = 0 \\ \quad \quad \quad I(y) \geq 0 \end{array} \right\} \quad (4.18)$$

where y is a set of design variables used to define a scalar objective $\phi[y]$ that is subject to a set of equality constraints $E(y)$ and a set of inequality constraints $I(y)$. The design variables y will be defined shortly.

For the sake of simplicity, let us first consider a single phase optimal control problem with free parameters. This approach assumes that the duration of the trajectory is unity. Often, this requires a scaling of the state equations using the same method previously illustrated by equations 4.7 through 4.9.

The transformation process begins with the discretization of the state equations into N equally spaced intervals resulting in $N+1$ nodes. Since the duration of the trajectory is unity, the time step between nodes is

$$\Delta t = \frac{1}{N} \quad (4.19)$$

Therefore, the time at each of the nodes is given by

$$t_i = \frac{i-1}{N}, \quad i = 1, \dots, N+1 \quad (4.20)$$

The design variables y to be optimized in this approach are the values of the states $x_i \in \mathcal{R}^n$ at the $N+1$ nodes, the values of the controls $u_i \in \mathcal{R}^m$ at the N nodal midpoints and the free parameters $z \in \mathcal{R}^j$. The ordering of the design variables is

$$y = [x_1 \ u_1 \ x_2 \ u_2 \ \cdots \ x_N \ u_N \ x_{N+1} \ z]^T \quad (4.21)$$

The objective function to be minimized for a single phase problem is given by

$$\mathcal{J} = \mathcal{J}(x_1, x_{N+1}, z) \quad (4.22)$$

Using a second-order, mid-point integration rule, the state equations produce the following system of equality constraints

$$x_{i+1} - x_i - \frac{1}{N}f(\bar{x}_i, u_i, z) = 0; \quad i = 1, \dots, N \quad (4.23)$$

where

$$\bar{x}_i = \frac{1}{2}(x_i + x_{i+1}) \quad (4.24)$$

Another set of equality constraints are the boundary conditions for the state equations which are of the form

$$\Psi(x_1, x_{N+1}, z) = 0 \quad (4.25)$$

State/control inequality constraints are of the form

$$\begin{bmatrix} \mathcal{C}_i(\bar{x}_1, u_1, z) \\ \mathcal{C}_i(\bar{x}_2, u_2, z) \\ \vdots \\ \mathcal{C}_i(\bar{x}_N, u_N, z) \end{bmatrix} \geq 0 \quad i = 1, \dots, n_c \quad (4.26)$$

where n_c is the number of state/control constraints. Like the discretized state equations, the state/control inequality constraints are enforced at the N nodal mid-points. The state-only inequality constraints are of the form

$$\begin{bmatrix} \mathcal{S}_i(x_1, z) \\ \mathcal{S}_i(x_2, z) \\ \vdots \\ \mathcal{S}_i(x_{N+1}, z) \end{bmatrix} \geq 0 \quad i = 1, \dots, n_S \quad (4.27)$$

where n_S is the number of state only constraints. Finally, free parameter inequality constraints expressed as

$$\mathcal{P}(z) \geq 0 \quad (4.28)$$

may also exist.

When integral cost expressions such as

$$\mathcal{J} = \int_0^1 \mathcal{L}(x, u, z) d\tau \quad (4.29)$$

must be addressed, the cost function is defined as a state. The state equation for this new state is

$$\dot{x}_{\mathcal{J}} = \mathcal{L}(x, u, z) \quad (4.30)$$

Now consider a multiple phase optimal control problem. The state equations for an L phase problem are expressed as

$$\dot{x}_k = f_k(x_k, u_k, z) \quad k = 1, \dots, L \quad (4.31)$$

where $x_k \in \mathcal{R}^{n_k}, u_k \in \mathcal{R}^{m_k}$ and $z \in \mathcal{R}^j$. After first scaling these equations such that the duration of each phase is unity, the equations are discretized into N_k equally spaced intervals. The NLP problem is formulated as in 4.18, except the design variables y are now ordered as

$$y = [y_1 \ y_2 \ \cdots \ y_L \ z]^T \quad (4.32)$$

where the design variables for the k th phase are

$$y_k = [x_{1k} \ u_{1k} \ x_{2k} \ u_{2k} \ \cdots \ x_{N_k k} \ u_{N_k k} \ x_{N_k+1k}]^T \quad (4.33)$$

Denoting the initial and final values of the states for the k th phase by x_{1k} and $x_{N_k k}$ respectively, the performance index is expressed as

$$\mathcal{J} = \mathcal{J}[x_{11}, x_{N_1 1}, x_{12}, x_{N_2 2}, \cdots, x_{1L}, x_{N_L L}, z] \quad (4.34)$$

Using the same mid-point integration rule, the state equations yield the following set of equality constraints

$$\left. \begin{aligned} x_{i+11} - x_{i1} - f(\bar{x}_{i1}, u_{i1}, z)/N_1 &= 0; & i = 1, \dots, N_1 \\ x_{i+12} - x_{i2} - f(\bar{x}_{i2}, u_{i2}, z)/N_2 &= 0; & i = 1, \dots, N_2 \\ &\vdots \\ x_{i+1L} - x_{iL} - f(\bar{x}_{iL}, u_{iL}, z)/N_L &= 0; & i = 1, \dots, N_L \end{aligned} \right\} \quad (4.35)$$

The boundary conditions now take the form

$$\Psi[x_{11}, x_{N_1 1}, x_{12}, x_{N_2 2}, \cdots, x_{1L}, x_{N_L L}, z] = 0 \quad (4.36)$$

The state/control inequality constraints for the k th phase are described as

$$C_k = \begin{bmatrix} C_i(\bar{x}_{1k}, u_{1k}, z) \\ C_i(\bar{x}_{2k}, u_{2k}, z) \\ \vdots \\ C_i(\bar{x}_{N_k k}, u_{N_k k}, z) \end{bmatrix} \geq 0 \quad i = 1, \dots, n_{Ck} \quad (4.37)$$

Similarly, the state-only inequality constraints for the k th phase are

$$\mathcal{S}_k = \begin{bmatrix} \mathcal{S}_i(x_{1k}, z) \\ \mathcal{S}_i(x_{2k}, z) \\ \vdots \\ \mathcal{S}_i(x_{N_k+1k}, z) \end{bmatrix} \geq 0 \quad i = 1, \dots, n_{C_k} \quad (4.38)$$

The inequality constraints are concatenated in the same manner as the state equation equality constraints yielding the two sets of inequality constraints

$$\mathcal{C} = \begin{bmatrix} \mathcal{C}_1 \\ \mathcal{C}_2 \\ \vdots \\ \mathcal{C}_L \end{bmatrix} \quad \mathcal{S} = \begin{bmatrix} \mathcal{S}_1 \\ \mathcal{S}_2 \\ \vdots \\ \mathcal{S}_L \end{bmatrix} \quad (4.39)$$

Free parameter inequality constraints of the form 4.28 may also be included. This approach is not self-starting. An initial guess is required to start an iterative solution process. The Fortran code NPSOL [8] was selected to solve the NLP problem. In appendix B, the codes that provided the skeleton of this method are described in detail.

4.3 Algorithm Performance

As a brief illustration of the algorithmic performance of NPSOL and the discretized problem representation described above, a simple problem will be solved. The solution will then be compared to the closed-form solution.

The double integrator problem is posed as follows :

Minimize the cost function

$$\mathcal{J} = \int_0^1 \frac{u^2}{2} dt \quad (4.40)$$

subject to the differential constraints

$$\left. \begin{aligned} \dot{x}_1 &= x_2; & x_1(0) &= 1 \\ \dot{x}_2 &= u; & x_2(0) &= 0 \end{aligned} \right\} t \in [0, 1] \quad (4.41)$$

and the boundary conditions or terminal constraints

$$\left. \begin{aligned} \Psi_1 &: x_1(1) - 1 = 0 \\ \Psi_2 &: x_2(1) = 1 \end{aligned} \right\} \quad (4.42)$$

The integral cost function is addressed as in 4.29 and 4.30. The resulting cost function is

$$\mathcal{J} = x_3(1) \quad (4.43)$$

which is subject to the state equations

$$\left. \begin{aligned} \dot{x}_1 &= x_2; & x_1(0) &= 1 \\ \dot{x}_2 &= u; & x_2(0) &= 0 \\ \dot{x}_3 &= \frac{1}{2}u^2 & x_3(0) &= 0 \end{aligned} \right\} t \in [0, 1] \quad (4.44)$$

the terminal constraints remain the same. The closed-form solution to this problem is

$$\left. \begin{aligned} x_1(t) &= 3t^3 - 4t^2 + 1 \\ x_2(t) &= 9t^2 - 8t \\ x_3(t) &= 54t^3 - 72t^2 + 32t \\ u(t) &= 18t - 8 \end{aligned} \right\} \quad (4.45)$$

The optimal value of the objective function is 14.

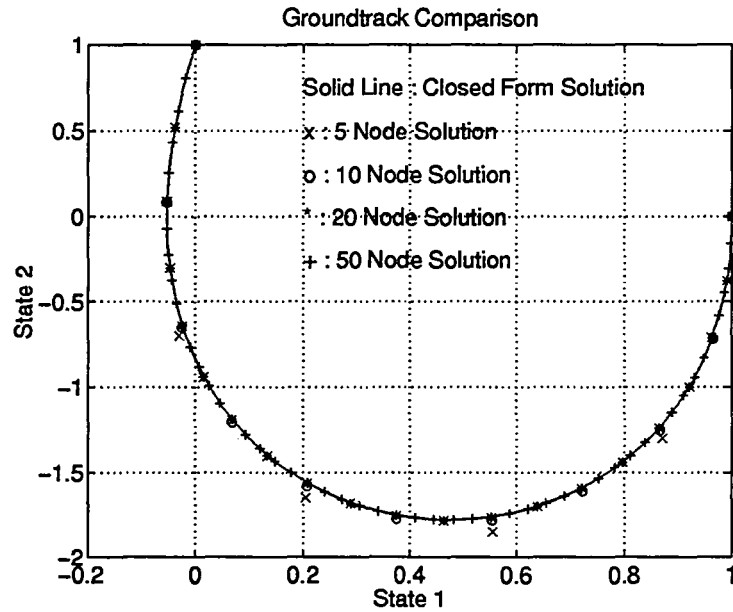


Figure 4.2: Ground-track Comparison

Solutions for this problem were also found for discretization intervals of $N = (5, 10, \text{ and } 20)$. Figure 4.2 shows the ground-tracks of the numerical solutions in comparison to 4.45. In table 4.1 results from the three different nodal densities studied are compared. As the example problem illustrates, the accuracy of this algorithm is enhanced by increasing the nodal density. As expected, as the nodal density is increased, the computational effort also increases. Thus, a trade-off must be made between desired accuracy and acceptable computational effort.

Table 4.1: Numerical Approach Results

Discretization Intervals	5	10	20	50
Design Variables	23	43	83	203
Iterations	15	24	34	27
Cost Function Evaluations	20	55	44	39
CPU Time, sec	0.5	2.7	20.4	203.1
Optimal Cost	14.5625	14.1364	14.0338	14.0054

Chapter 5

Abort Maneuvers

In this section the abort capabilities of the SSTO vehicle are examined. Each of the optimal control problems used in this investigation are described. Results for each problem are presented after the problem is described.

5.1 Baseline Performance Problem Description

Before examining the abort maneuvers, a baseline for performance must be created. For this study, the baseline will be a maximum mass to orbit ascent trajectory for a vehicle with a full complement of engines. The target orbit is a 50 by 100 nmi orbit with an inclination of 51.6° .

If m_f is the mass of the vehicle at orbit insertion, the baseline trajectory is found by minimizing the objective function

$$\mathcal{J} = -m_f \tag{5.1}$$

Note that minimizing $-m_f$ is equivalent to maximizing m_f . The state equations for this problem were previously described in 3.1. The boundary conditions for this problem are

$$\left. \begin{aligned}
v_0 &= 0.1 && \text{ft/s} \\
h_0 &= 0 && \text{ft} \\
m_0 &= 2383.43 && \text{klbm} \\
\theta_0 &= -80.71 && \text{deg} \\
\phi_0 &= 28.47 && \text{deg} \\
v_f &= 25852 && \text{ft/s} \\
\gamma_f &= 0 && \text{deg} \\
h_f &= 3.03805 && \text{ft} \\
i_f &= 51.6 && \text{deg}
\end{aligned} \right\} \quad (5.2)$$

As shown in [11], the final inclination i_f can be found with

$$i_f = \cos^{-1} \left(\frac{v_f \cos \gamma_f \cos \phi_f \cos \psi_f + \omega (h_f + r_e) \cos^2 \phi}{\sqrt{(v_f \cos \gamma_f \cos \psi_f + (h_f + r_e) \omega \cos \phi)^2 + (v_f \cos \gamma_f \sin \psi_f)^2}} \right) \quad (5.3)$$

The initial flight-path and heading angles are designated as free variables, thus neglecting the brief and highly constrained motion required to clear the launch pad.

The state/control inequality constraints for this problem are

$$\left. \begin{aligned}
0.25 &\leq \eta \leq 1.09 \\
|\alpha| &\leq 45^\circ \\
|F_N| &\leq 3.81232e + 05 \text{ lbf} \\
|A| &\leq 3g_0
\end{aligned} \right\} \quad (5.4)$$

where A is the acceleration of the vehicle, g_0 denotes the gravitational acceleration at sea level, and F_N is the normal force, given by

$$F_N = 1/2 \rho v^2 S c_N \quad (5.5)$$

where the normal force coefficient c_N is

$$c_N = c_D \sin \alpha + c_L \cos \alpha \quad (5.6)$$

The state-only inequality constraints are

$$\left. \begin{aligned} h &\geq 0 && \text{ft} \\ m &\geq m_{dry} \\ q &\leq 1000 && \text{psf} \\ M &\geq 0 \\ |\gamma| &\leq 90^\circ \end{aligned} \right\} \quad (5.7)$$

where the dynamic pressure q is given by

$$q = 1/2\rho v^2 \quad (5.8)$$

Since this is a free time problem, the duration of the trajectory τ is a free parameter. The state equations 3.1 must be scaled by this parameter. The free parameter inequality constraint shown below guarantees that time will monotonically increase.

$$\tau \geq 0 \quad (5.9)$$

5.2 Baseline Performance Results

The resulting state trajectories for the baseline performance problem are shown in Figures 5.1 through 5.6. The mass lifted into orbit is 286.74 klbm which is 12 percent of the mass of the vehicle at lift-off. If one assumes that all of the propellant is used during the ascent, the corresponding maximum payload is 80.25 klbm. The time of flight is 370 seconds.

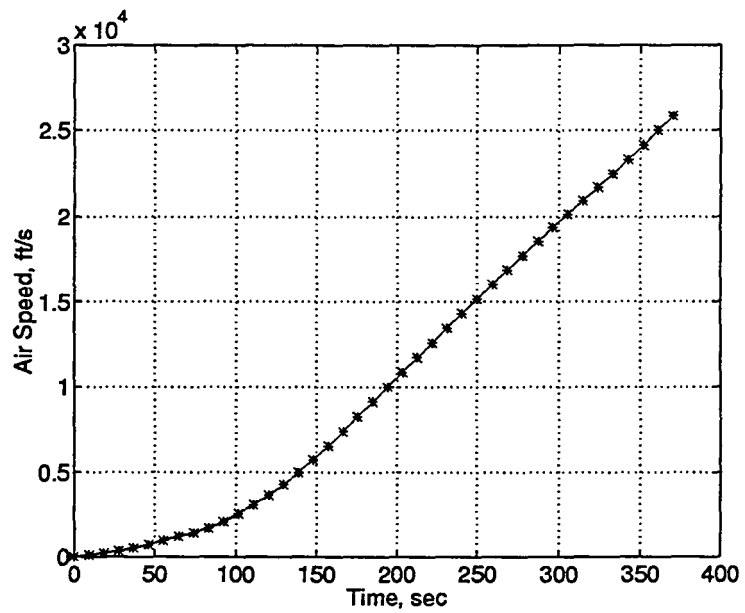


Figure 5.1: Baseline Ascent Trajectory : Air Speed

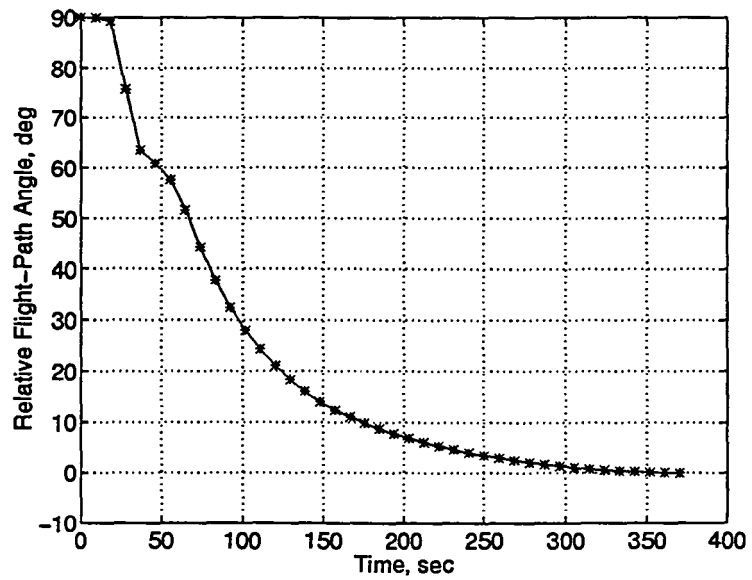


Figure 5.2: Baseline Ascent Trajectory : Relative Flight-Path

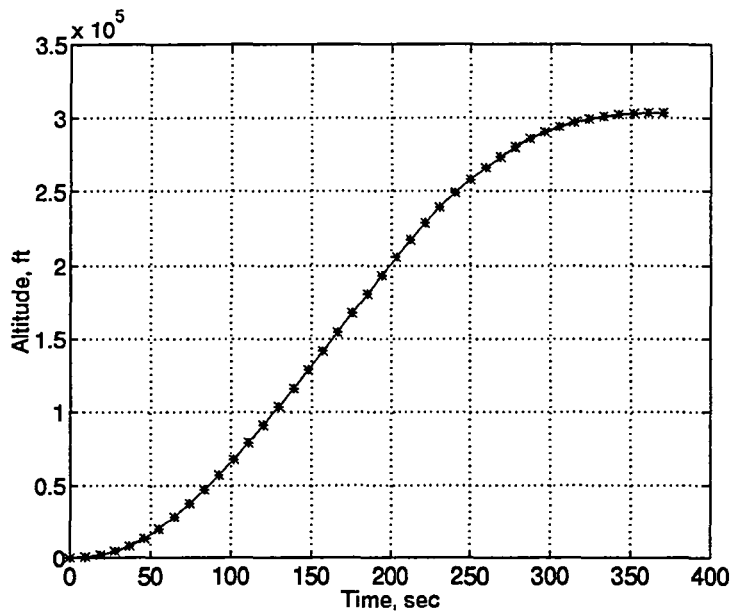


Figure 5.3: Baseline Ascent Trajectory : Altitude

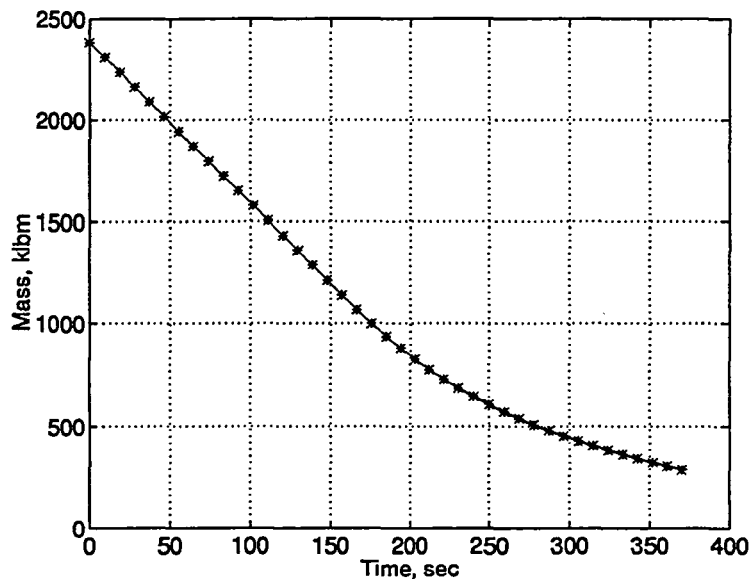


Figure 5.4: Baseline Ascent Trajectory : Mass

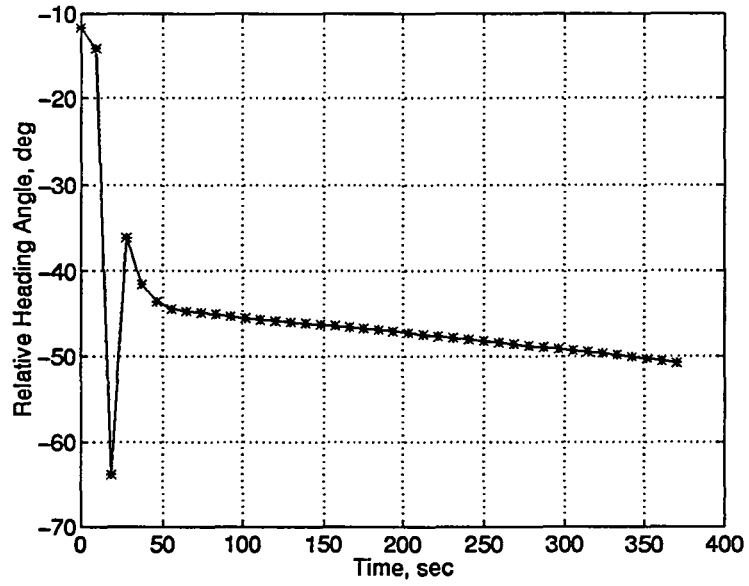


Figure 5.5: Baseline Ascent Trajectory : Relative Heading

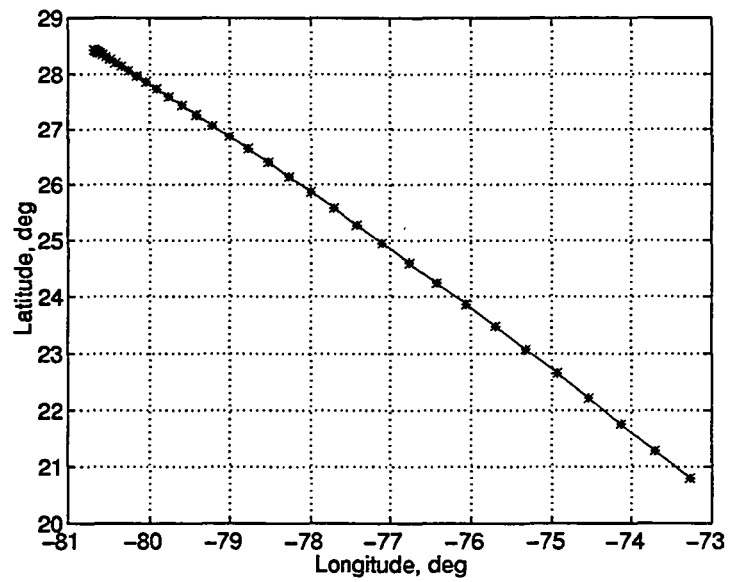


Figure 5.6: Baseline Ascent Trajectory : Groundtrack

The control histories for this ascent are illustrated by Figures 5.7 through 5.9. The throttle history shows that the vehicle flies full throttle for most of the first 160 seconds of the ascent. At this time the vehicle begins to reduce the throttle to prevent the violation of the acceleration limit. A slight reduction in throttle is seen 50 seconds after launch. This reduction is to prevent the violation of the normal force constraint. Figure 5.10 shows when various inequality constraints become active during the ascent. In this figure, active constraints are represented with lines passing through asterisks.

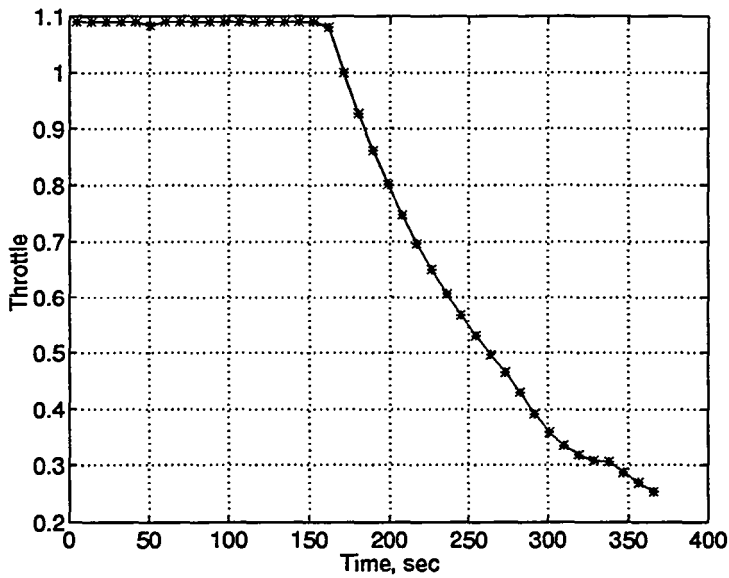


Figure 5.7: Baseline Ascent Trajectory : Throttle

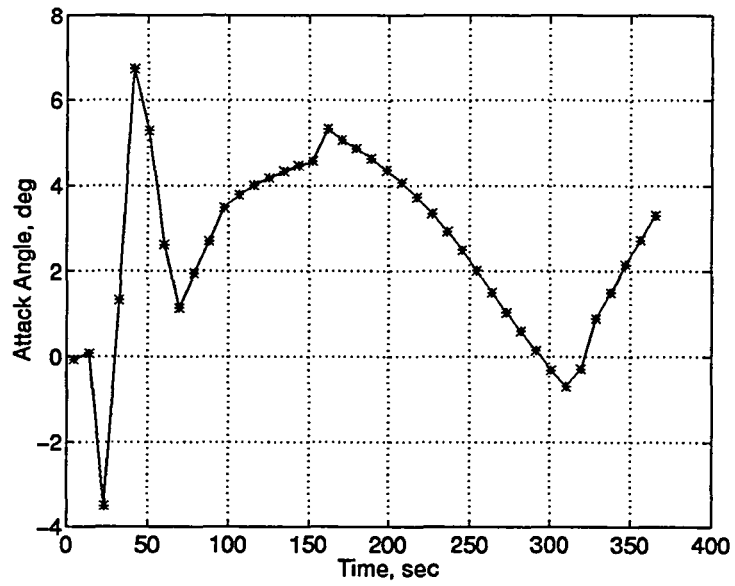


Figure 5.8: Baseline Ascent Trajectory : Attack Angle

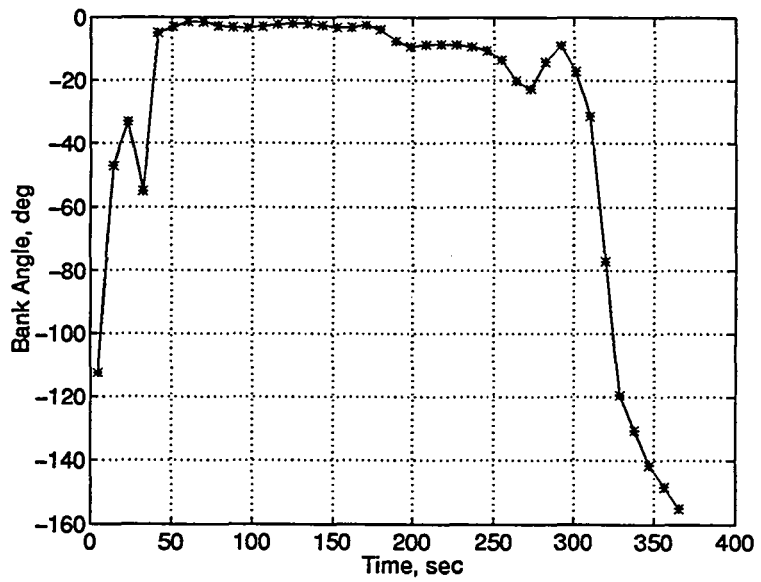


Figure 5.9: Baseline Ascent Trajectory : Bank Angle

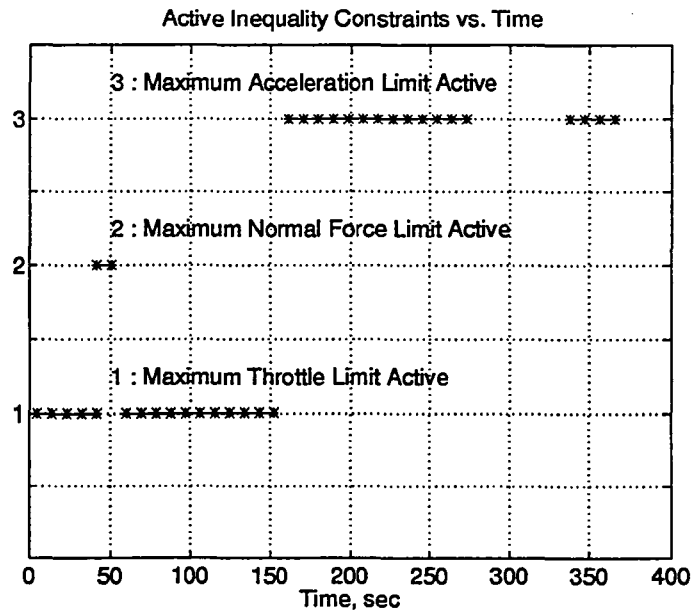


Figure 5.10: Active Inequality Constraints in Baseline Ascent

In Figure 5.11 the attack angle is plotted as a function of mach number. This figure shows that as the vehicle travels through the transonic mach region the magnitude of the attack angle is reduced. Figure 5.12 shows the drag profile for the trajectory. The maximum value of drag is 845 klbf and occurs 70 seconds after lift-off when the vehicle is traveling at mach 1.18. Since the drag acting on the vehicle reaches a maximum in the transonic region (denoted by asterisks), the vehicle must fly with low angles of attack in order to minimize drag and increase performance.

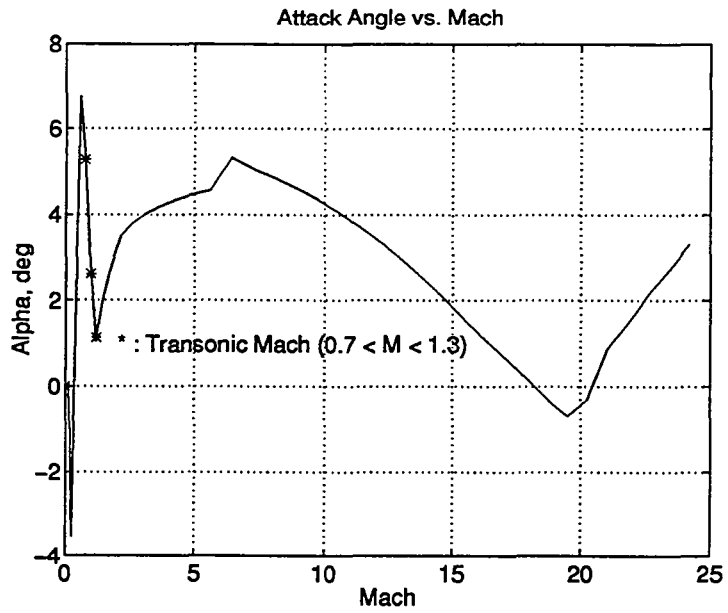


Figure 5.11: Minimizing Attack Angle in Transonic Region

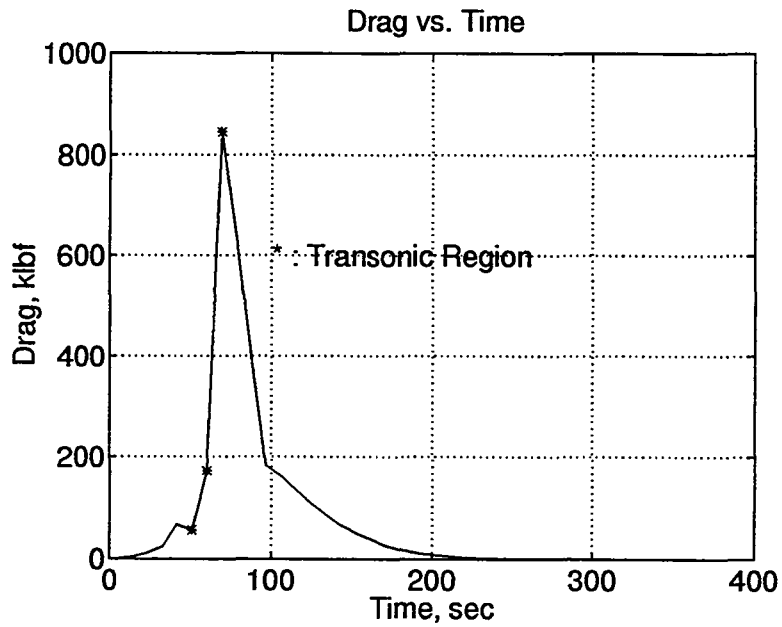


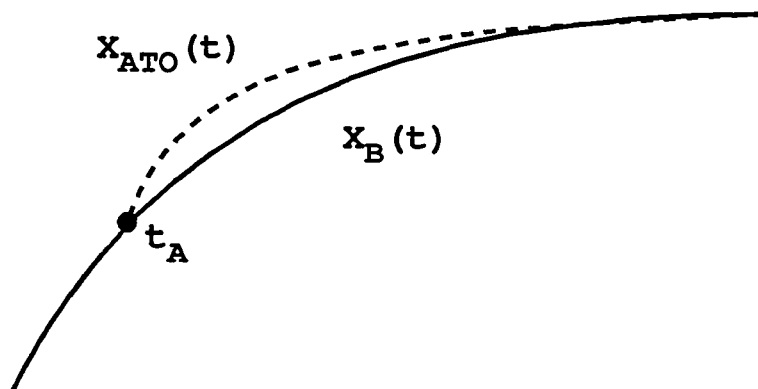
Figure 5.12: Baseline Ascent Trajectory : Drag Profile

5.3 ATO Maneuver Problem Descriptions

In this problem, the vehicle ascends to orbit by traveling along the previously described baseline trajectory. At time t_A after launch, the vehicle suffers an engine failure. The objective of this problem is to determine the loss in performance caused by an engine failure at time t_A . Single-engine and two-engine-out scenarios are studied.

As in the baseline trajectory problem, the performance index for this problem is

$$\mathcal{J} = -m_f \tag{5.10}$$



The state equations 3.1 are modified to account for the appropriate reduction in the number of engines $N_{engines}$. In Figure 5.3 provides an illustration of the ATO maneuver problem. In this figure, the baseline state trajectory is denoted as $x_B(t)$. Referring to this figure the boundary conditions for this problem are

$$\left. \begin{aligned}
v_0 &= v_B(t_A) \\
\gamma_0 &= \gamma_B(t_A) \\
h_0 &= h_B(t_A) \\
m_0 &= m_B(t_A) \\
\psi_0 &= \psi_B(t_A) \\
\theta_0 &= \theta_B(t_A) \\
\phi_0 &= \phi_B(t_A) \\
v_f &= 25852 \quad \text{ft/s} \\
\gamma_f &= 0 \quad \text{deg} \\
h_f &= 3.03805e + 05 \quad \text{ft} \\
i_f &= 51.6 \quad \text{deg}
\end{aligned} \right\} \quad (5.11)$$

Since the baseline ascent trajectory is represented by a discrete number of states, interpolation is used to determine the values of $x_B(t_A)$ for which data points do not exist.

The state/control and state-only inequality constraints are the same as those enforced in the baseline trajectory previously given in 5.4 and 5.7. Like the the baseline trajectory problem, this problem is a free time problem. As always, the state equations must be scaled by the duration of the trajectory τ which is represented by a free parameter. The free parameter inequality constraint

$$\tau \geq 0 \quad (5.12)$$

is added to prevent the time scale from become negative.

5.4 ATO Maneuver Results

Figure 5.13 shows the maximum payload mass that can be delivered to orbit as a function of the time of engine failure t_A . Results from single-engine and two-engine-out scenarios are shown.

In this figure, initial results for the single engine out scenario are labeled **Single-Engine-Out 1**. These results were obtained as t_A was varied from 0 to 100 seconds after launch in 10 second intervals. As t_A was varied, the solution for the problem with current value of t_A served as the initial guess for the next problem with t_A incremented. These results suggest that a slight decrease in performance occurs as t_A is increased from 50 to 60 seconds after launch. The large increase in performance shown as t_A is varied from 80 to 90 seconds after launch hints that the “solutions” for engine failure times in the interval $60 \leq t_A \leq 80$ are local minima.

The **Single-Engine-Out 2** results were obtained by walking the time of engine failure from 90 to 40 seconds after launch in 5 second intervals. Again, each solution served as the initial guess for the problem with the subsequent value of t_A . The improved performance shown by the **Single-Engine-Out 2** solutions supports the previous intuition that the **Single-Engine-Out 1** solutions for this same time range are local minima. Note that since **Single-Engine-Out 2** results were not determined to be the global minimum (a difficult task for most optimal control problems), these results should also be categorized as local minima. Both sets of solutions are feasible solutions.

Solutions for two-engine-out cases were found for engine failure times in the interval $50 \leq t_A \leq 100$. Solutions could not be found for engine failure times below 50 seconds after launch. If traveling on the baseline ascent trajectory, a vehicle with two failed engines has a thrust to weight ratio less than 1 until 25 seconds after lift-off. The thrust to weight ratio remains inadequate for the two-engine-out ATO maneuvers until the conditions 50 seconds after launch.

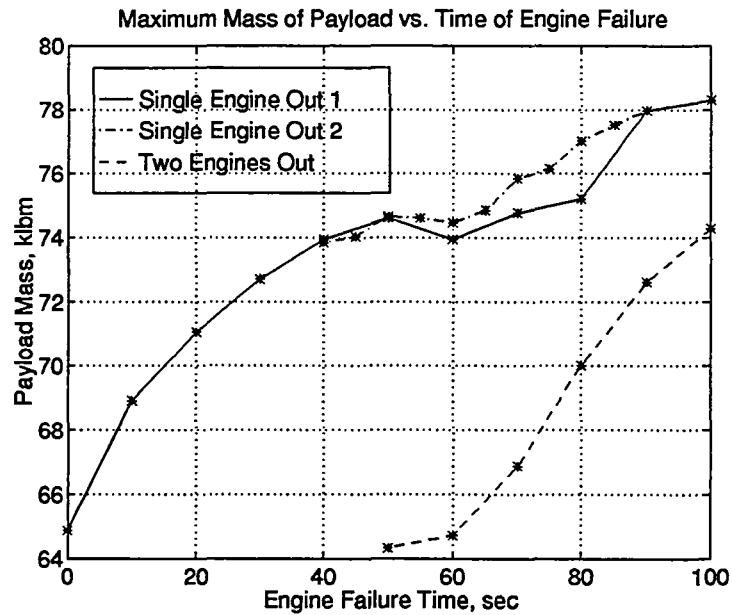


Figure 5.13: ATO Maneuver Performance

Further investigation of the single-engine-out results shows that a decrease in performance occurs as the time of engine failure varies from 50 to 60 seconds after launch. As Figure 5.12 previously illustrated, the vehicle begins to enter the transonic region during this time frame. Figure 5.14 shows the two drag profiles for these to single-engine-out ATO maneuvers. This figure shows that the 60 second case flies with more drag than the 50 second case resulting in the decreased performance.

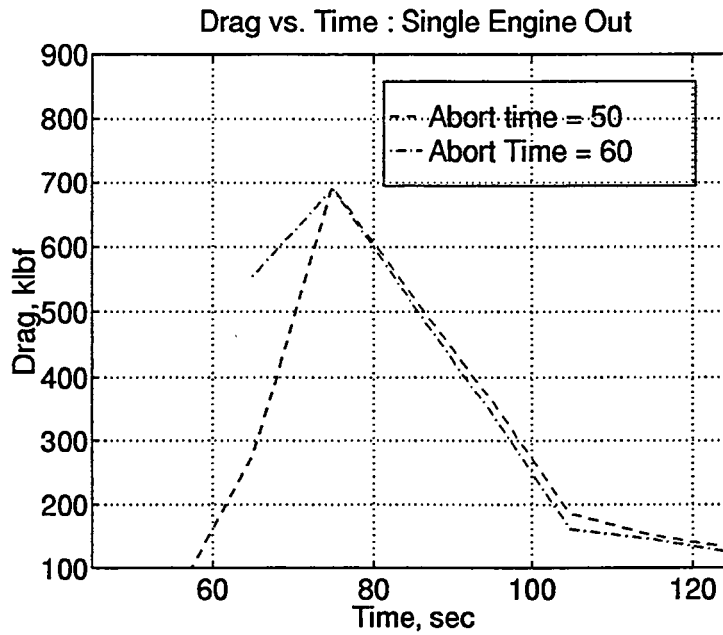


Figure 5.14: Drag Profiles for ATO Maneuvers Initiated at 50 and 60 Seconds After Launch

Figure 5.15 shows that single-engine and two-engine-out ATO maneuvers initiated at 60 seconds after launch fly more lofting trajectories than the baseline trajectory. Note that the two-engine-out scenario flies a more lofting trajectory than the single-engine-out scenario. To investigate this behavior, examine the expression for $\frac{dh}{dv}$, approximated by

$$\frac{dh}{dv} \cong mv \sin \gamma / (T \cos \alpha - D) \quad (5.13)$$

Because of the engine failure(s), $T \cos \alpha$ is larger for the baseline ascent than for the ATO trajectories. As a result $\frac{dh}{dv}$ is larger for the ATO trajectories.

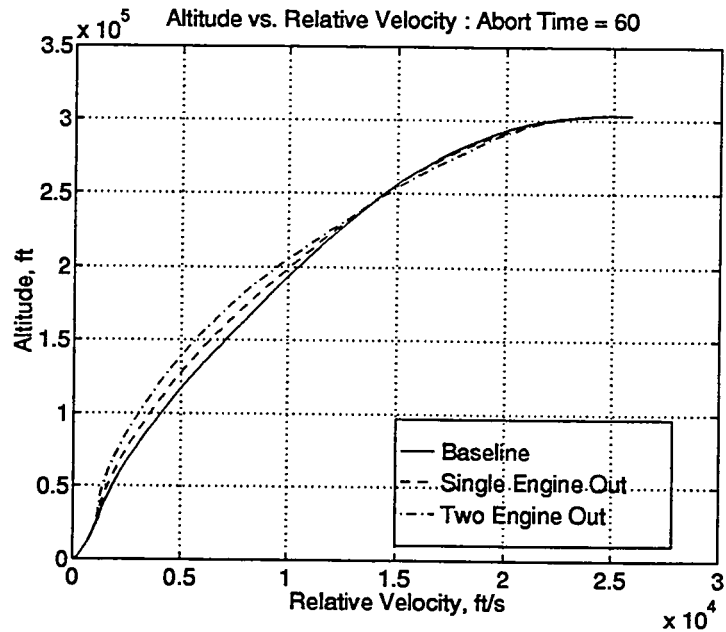


Figure 5.15: Lofting of ATO Maneuvers Initiated 60 Seconds After Launch

Figure 5.16 shows the attack angle profiles for the for the same two scenarios. This figure shows that the vehicle must fly with higher attack angles after engine failure occurs.

Figure 5.17 illustrates mass as a function of time for the same scenarios. As expected the single-engine-out scenario out performs the two-engine-out scenario. Unsurprisingly, the time of flight for the two-engine-out scenario is longer than the single-out-scenario, since the vehicle has even less thrusting capability.

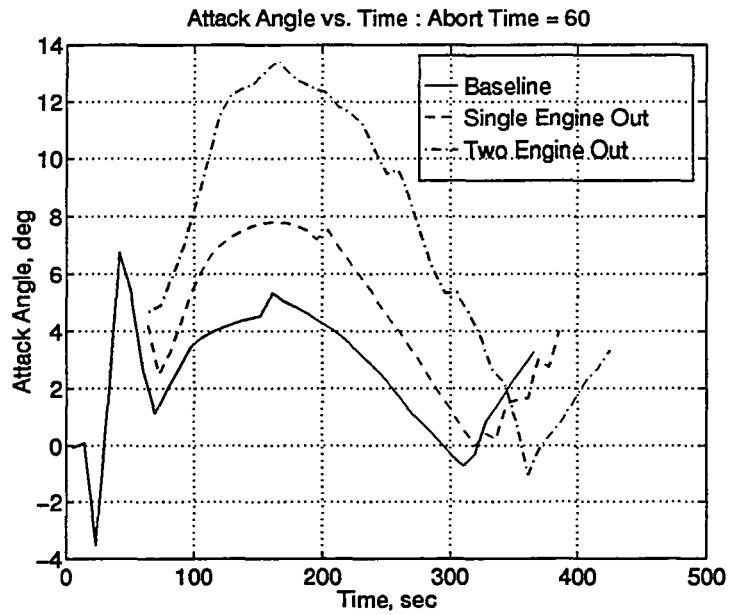


Figure 5.16: Attack Angle Profiles for ATO Maneuvers Initiated 60 Seconds After Launch

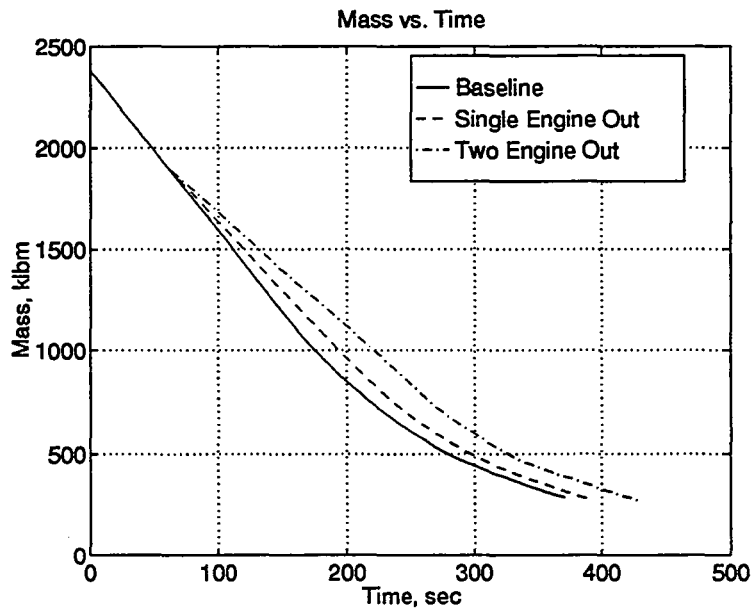


Figure 5.17: Mass Profiles for ATO Maneuvers Initiated 60 Seconds After Launch

Finally, the throttle profiles depicted in Figure 5.18 illustrate that the reduction thrust due to engine failure is compensated for by maintaining the throttle at the maximum value longer.

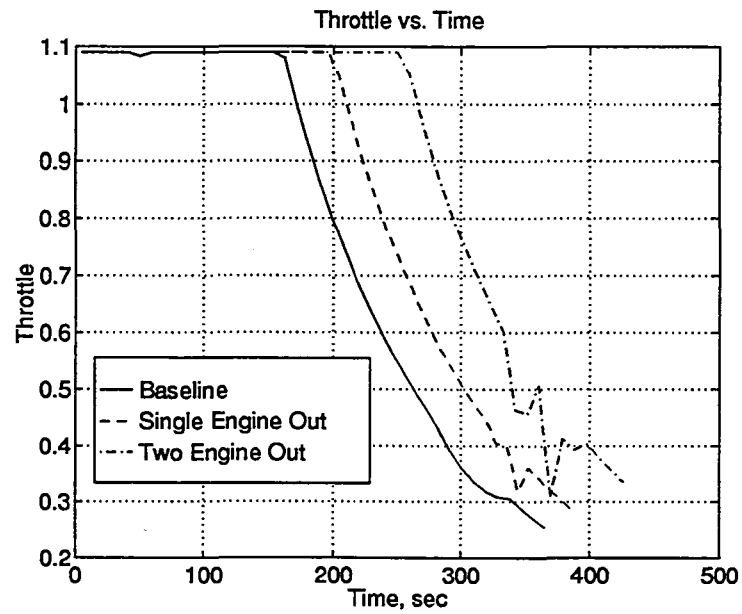


Figure 5.18: Throttle Profiles for ATO Maneuvers Initiated 60 Seconds After Launch

5.5 RTLS Maneuver Problem Descriptions

Several problems are investigated for the return to launch site maneuver. Each formulation consists of two phases and thus utilizes the multiple phase capability of the numerical approach previously described. Like the ATO maneuver problem, the RTLS maneuvers are initiated from fixed points on the baseline ascent trajectory. The first phase is designed to empty the propellant from the vehicle tanks. During the second phase, the lightened vehicle flies back to the landing site. Figure 5.19 illustrates the different phases of the RTLS maneuver.

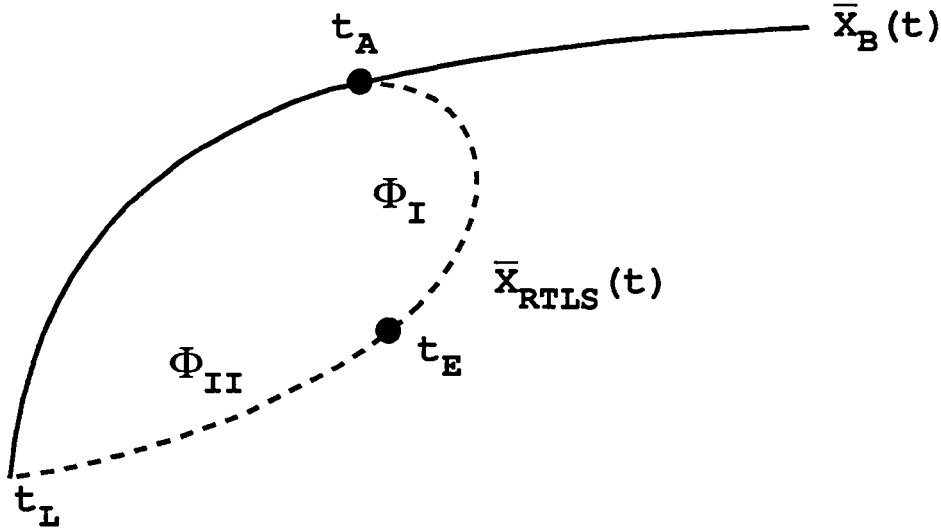


Figure 5.19: RTLS Phases

5.5.1 Maximize Time of Abort

The objective of this problem is to determine the maximum time after launch that a vehicle suffering from an engine failure can return to the launch site. This “point of no return” will be found for a vehicle carrying the nominal payload mass of 20 klbm. If the engine failure occurs at time t_A after launch, the performance index for this problem is

$$J = -t_A \quad (5.14)$$

The state equations 3.1 are modified to reflect the reduction in the number of engines. If the baseline trajectory is denoted by $x_B(t)$, the boundary conditions for this problem are

$$\left. \begin{aligned} v_0 &= v_B(t_A) \\ \gamma_0 &= \gamma_B(t_A) \\ h_0 &= h_B(t_A) \\ m_0 &= m_B(t_A) \\ \psi_0 &= \psi_B(t_A) \\ \theta_0 &= \theta_B(t_A) \\ \phi_0 &= \phi_B(t_A) \\ v_f &= 524 && \text{ft/s} \\ \gamma_f &= 0 && \text{deg} \\ h_f &= 2000 && \text{ft} \\ m_f &= m_{dry} + m_{payload} \\ \psi_f &= -300 && \text{deg} \\ \theta_f &= -80.68 && \text{deg} \\ \phi_f &= 28.44 && \text{deg} \end{aligned} \right\} \quad (5.15)$$

where the final conditions represent typical landing conditions. The state/control inequality constraints for this problem are

$$\left. \begin{aligned} \Phi_I: \quad 0.25 &\leq \eta \leq 1.09 \\ \Phi_{II}: \quad 0.0 &\leq \eta \leq 0.0 \quad (i.e. \eta = 0 \rightarrow T = 0) \\ |\alpha| &\leq \alpha_{max} \\ |F_N| &\leq 3.81232e + 05 \text{ lbf} \\ |A| &\leq 3g_0 \end{aligned} \right\} \quad (5.16)$$

where the throttle limits are defined for each phase Φ and the maximum attack angle $\alpha_{max} \in [60^\circ, 90^\circ]$. Note that in the second phase, the throttle is constrained to zero. Therefore, the thrust must also be set to zero or the back pressure term A_{ep} will be incorrectly applied which may result in negative thrust. The state-only inequality constraints are

$$\left. \begin{aligned} h &\geq 0 \quad \text{ft} \\ m &\geq m_{dry} + m_{payload} \\ q &\leq 1000 \quad \text{psf} \\ M &\geq 0.3 \\ -90^\circ &\leq \gamma \leq 90^\circ \end{aligned} \right\} \quad (5.17)$$

where the mach number is constrained to be above the stall mach.

Three free parameters exist for this problem: the abort time t_A , the empty tank time t_E and the terminal or landing time t_L . Denoting the final time of the baseline ascent trajectory as t_{Bf} , the free parameter inequality constraints are

$$\left. \begin{aligned} 0 &\leq t_A \leq t_{Bf} \\ t_E &\geq t_A \\ t_L &\geq t_E \end{aligned} \right\} \quad (5.18)$$

5.5.2 Payload Returned To Launch Site

The results from the ATO maneuver study have shown that the subject SSTO vehicle has single-engine-out capability from the launch pad. The trade-off is a reduction in

the amount of mass that can be delivered to orbit. Operationally, this dictates the scenario for performing an RTLS maneuver. A RTLS maneuver should be performed if the payload mass is greater than that which can be delivered to orbit by an ATO maneuver. This assumes that an RTLS maneuver can be made with such a payload mass.

To test this assumption, the maximum and minimum amounts of payload that can be returned to the launch site are determined for specified times of engine failure t_A . For the maximum payload problem, the objective function is

$$\mathcal{J} = -m_{payload} \quad (5.19)$$

while for the minimum payload problem

$$\mathcal{J} = m_{payload} \quad (5.20)$$

Again, the state equations 3.1 are modified to reflect the reduction in the number of engines. The boundary conditions, state/control inequality constraints and state-only inequality constraints are the same as those previously given by 5.15, 5.16 and 5.17 respectively.

In these problems the free parameters are the payload mass $m_{payload}$, the empty tank time t_E and the terminal time t_L . Recall, the baseline ascent trajectory delivers a maximum payload of 80.25 klbm to orbit. If the maximum payload is denoted as $payload_{max}$, the free parameter inequality constraints for these problems are

$$\left. \begin{aligned} 0 &\leq m_{payload} \leq payload_{max} \\ t_E &\geq t_A \\ t_L &\geq t_E \end{aligned} \right\} \quad (5.21)$$

5.6 RTLS Maneuver Results

Investigating a single-engine-out scenario, the maximum time of abort was determined for a vehicle carrying the nominal payload of 20 klbm. Various attack angle limits α_{max} were examined. Figure 5.20 shows that the maximum time of abort decreases as the attack angle is more tightly constrained.

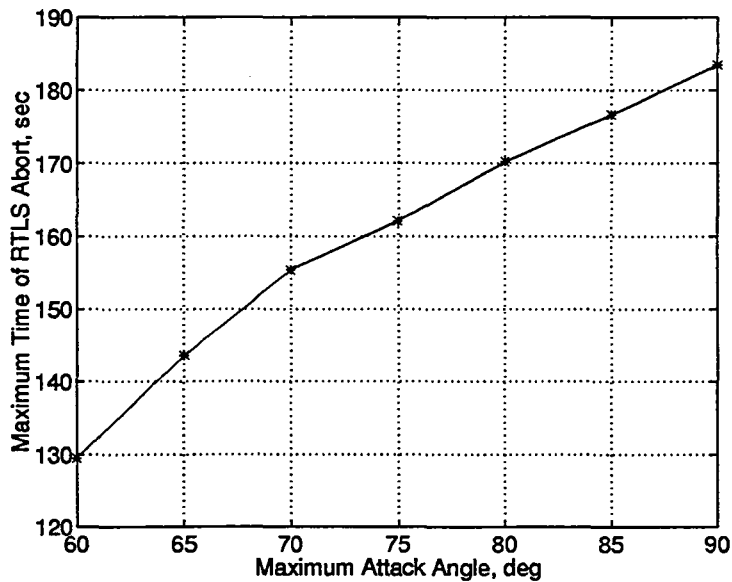


Figure 5.20: RTLS Maximum Abort Time Versus Maximum Attack Angle For Single Engine Out Scenario

To make the turn back toward the landing site, the vehicle must travel at reduced speeds to prevent exceeding critical structural loadings. The speed of the vehicle can be slowed by either decreasing the throttle or by increasing the drag acting on the vehicle. A vehicle flying with minimum throttle can only reduce speed by increasing drag which calls for high attack angles. As the attack angle is more tightly constrained, a final option for reducing the speed is chosen. This option is to initiate the abort maneuver sooner when the vehicle is traveling at speeds sufficiently slow to make the required turn.

Figure 5.21 plots altitude as a function of velocity for the maximum attack angle $\alpha_{max} = 90^\circ$ case. In this figure various times of interest are denoted with the letters

A-I. At A the abort is initiated at 183 seconds after launch. From A to B, the vehicle climbs to as to reduce the downrange distance from the abort site. From B to C, the vehicle speed is reduced by flying with the maximum attack angle as shown in Figure 5.22. At C, the turn towards the launch site has been completed as shown by Figure 5.23. From C to D, the vehicle empties its tanks by increasing its throttle as illustrated by Figure 5.24. This results in the climb shown in Figure 5.21. At D, the tanks are empty and the glide to the landing strip begins. During B to C and E to F the normal force inequality constraint is active. The vehicle climbs and reduces its attack angle (see Figure 5.22) to prevent the violation of this constraint. From G to H the vehicle loses excess energy by traveling in the high drag transonic region. Finally, at I the landing conditions are satisfied.

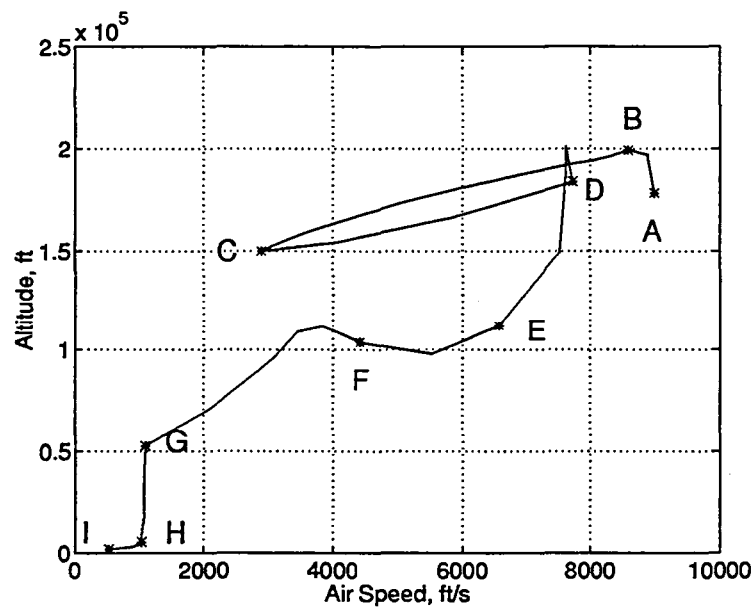


Figure 5.21: RTLS Max. Alpha = 90, Altitude vs Air Speed

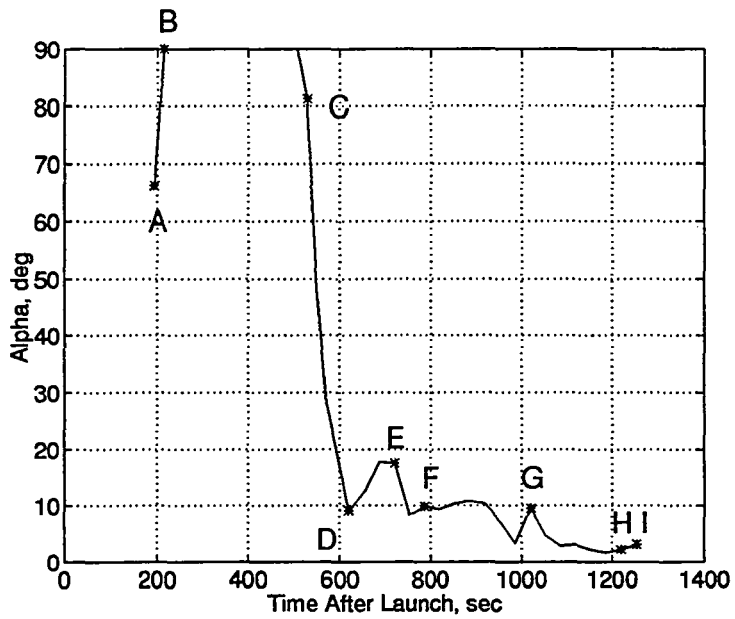


Figure 5.22: RTLS Max. Alpha = 90, Attack Angle vs Time After Launch

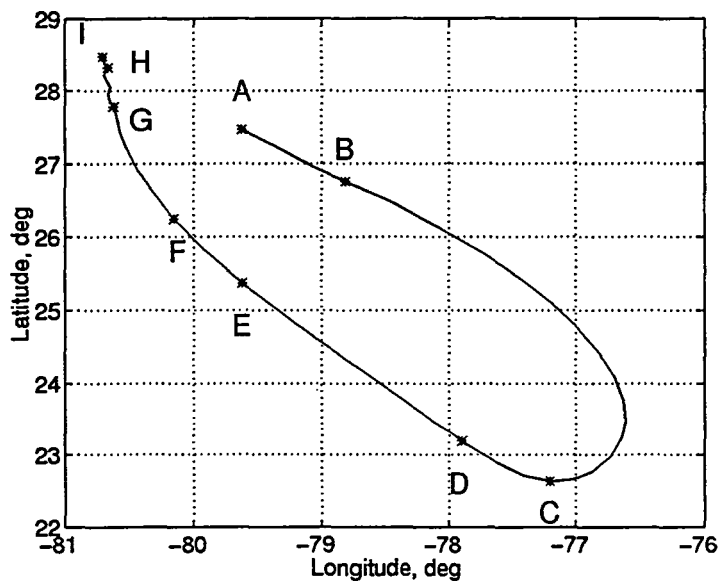


Figure 5.23: RTLS Max. Alpha = 90, Groundtrack

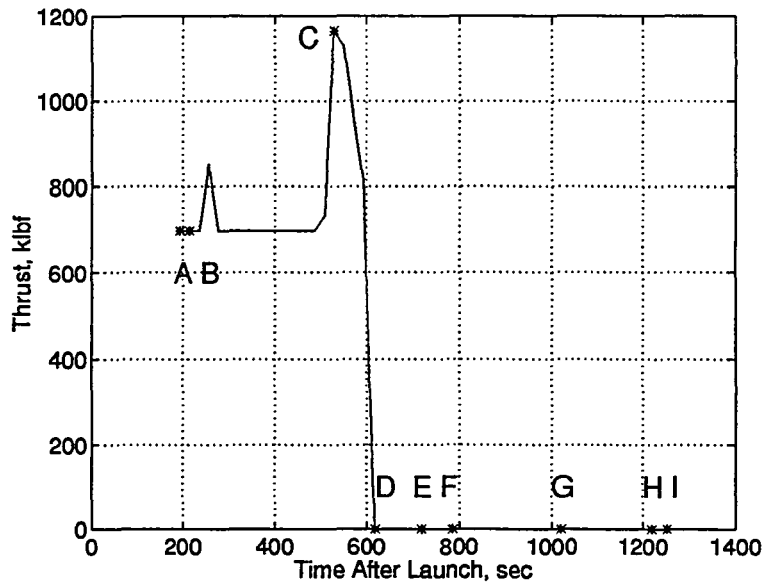


Figure 5.24: RTLS Max. Alpha = 90, Thrust Profile

Figure 5.25 illustrates the heading time history. This figure shows that the heading angle is slowly modulated between -220° and -300° as the vehicle approaches the landing site. This maneuvering assists in the removal of excess energy as the vehicle flies through the high drag transonic region.

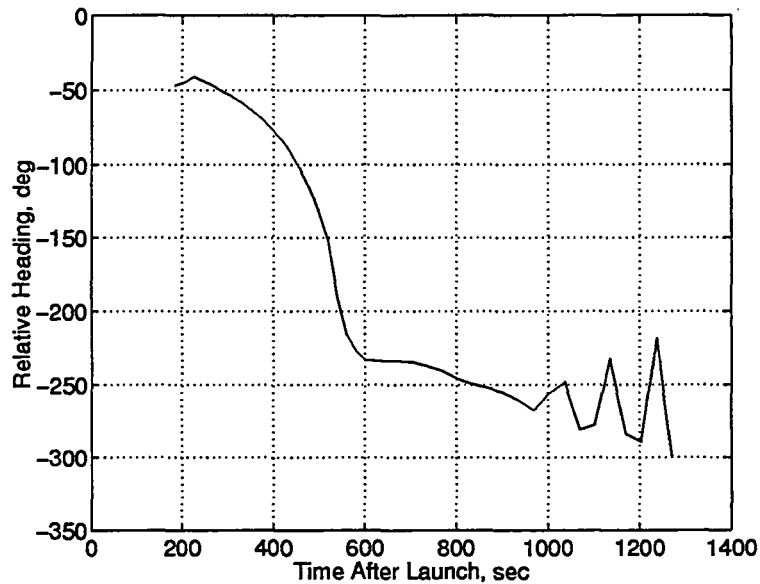


Figure 5.25: RTLS Max. Alpha = 90, Heading Angle History

Figures 5.26-5.28 show the RTLS air speed, altitude and groundtrack profiles for several values of α_{max} . For the 90° and 75° cases, the vehicle initiates the abort at a significantly higher speed than the 60° case. All three cases show that the vehicle initially climbs, but the 90° and 75° cases pull much larger attack angles to break off excess speed through increased drag, before beginning to turn. This results in the elongated groundtracks of Figure 5.28. In all three cases, the climb serves to keep the length of the glide back to the launch site to a manageable size, and to prevent the kinetic energy from becoming excessive.

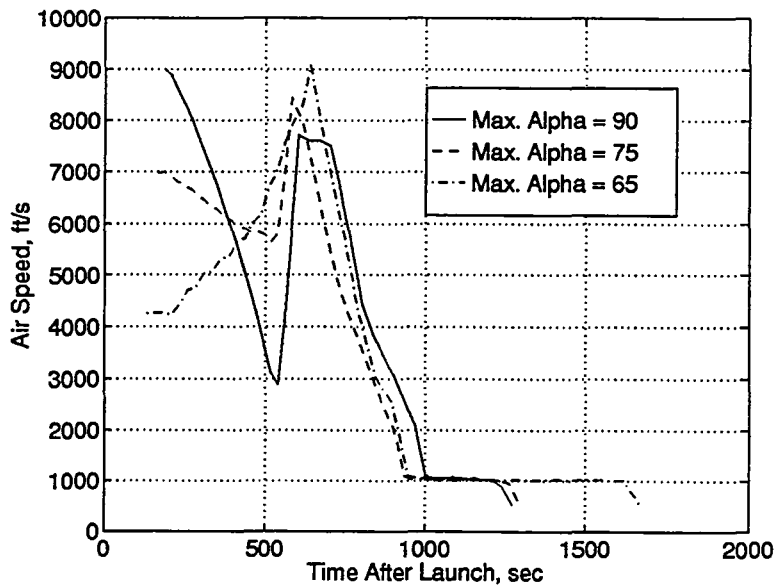


Figure 5.26: Maximum Abort Time RTLS Maneuvers : Relative Velocity Profile

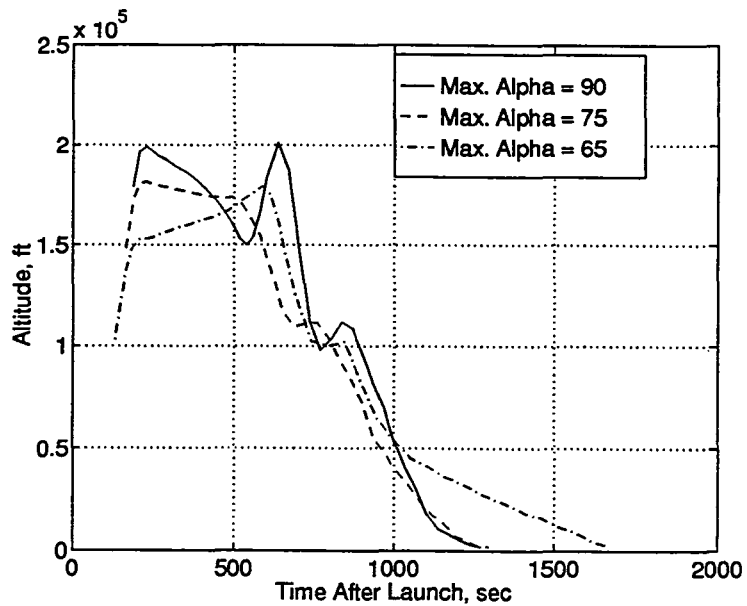


Figure 5.27: Maximum Abort Time RTLS Maneuvers : Altitude Profile

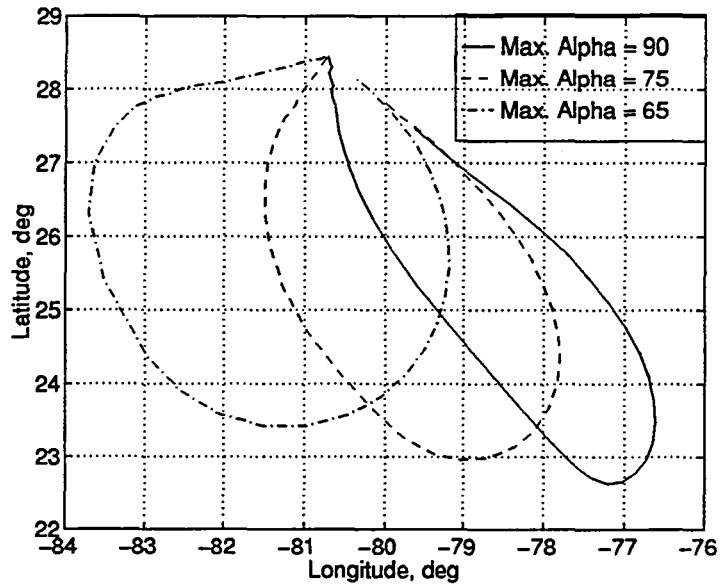


Figure 5.28: Maximum Abort Time RTLS Maneuvers : Ground-track

Figure 5.29 illustrates the attack angle histories for the three cases examined. All three profiles show that the vehicle flies at maximum attack angles until the turn toward the landing site has been made. For the 90° and 75° cases, the vehicle slows down by maximizing drag. In the 60° case, the vehicle burns off the excess propellant by climbing.

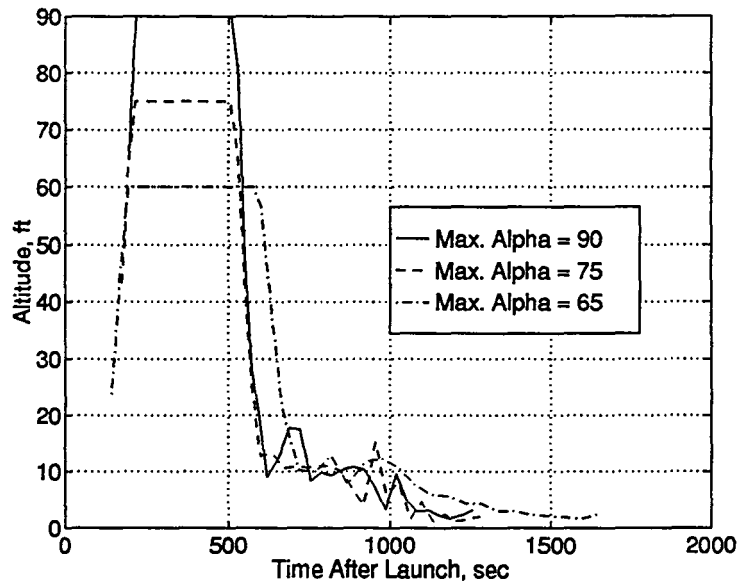


Figure 5.29: Maximum Abort Time RTLS Maneuvers : Attack Angle Profile

The throttle histories for the same three maximum attack angles are shown in Figure 5.30. Note that in the 75° and 60° cases, the throttle fluctuates during the initial phase of the flight. This appears to be a fairly typical case of chattering control, associated with linearly appearing controls (thrust) during deceleration with a quadratic drag polar. This figure stresses the important trade-off that is made between slowing the vehicle for the turn and decreasing the mass of the vehicle. The vehicle is attempting to simultaneously command speed, mass flow and flight-path angle rates which can only be physically realized in a time averaging sense.

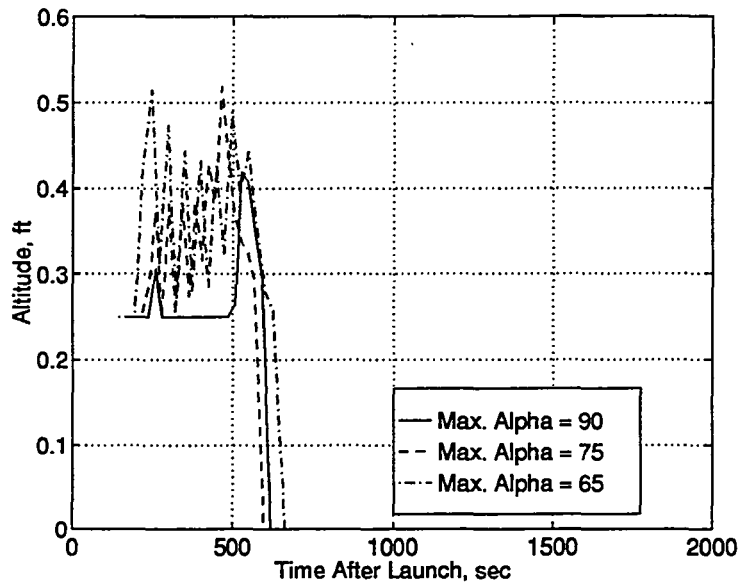


Figure 5.30: Maximum Abort Time RTLS Maneuvers : Throttle Profile

For RTLS maneuvers initiated at specified abort times, the maximum and minimum payload masses that could be returned to the launch site were determined. Single and two-engine-out scenarios were investigated. For each of the cases examined, the maximum payload mass that could be returned to the launch site was 80.25 klbm. This is the maximum payload mass that can be delivered to orbit by a vehicle with a full complement of engines.

Chapter 6

Summary

In this study, optimal control theory was employed to investigate the performance of abort to orbit (ATO) and return to launch site (RTL) maneuvers for a seven engine, winged-body single-stage to orbit (SSTO) vehicle which lifts-off vertically and lands horizontally. The maneuvers were initiated when the vehicle suffered an engine failure, while ascending to orbit along a maximum mass to orbit trajectory. Single-engine and two-engine out scenarios were studied. Different measures of performance were used for ATO and RTL maneuvers. The optimal control problems are solved in discretized form via a non-linear programming (NLP) method.

For the ATO maneuvers, the mass delivered to orbit was selected as the performance measure. For the single-engine-out scenario, ATO maneuvers were successfully made from abort times ranging for 0 to 100 seconds after launch. The corresponding payload mass delivered to orbit ranged from 65 to 78 klbm. In general, the performance increased as the abort time increased. Exceptions to this generalization occurred as the abort time was varied from 50 to 60 seconds after launch. During the time frame, the vehicle enters the high drag transonic mach region which limits the maneuverability of the vehicle. The loss of maneuverability restricts the ability of the vehicle to correct the ascent trajectory to compensate for the loss in thrust.

Two-engine-out ATO maneuvers were performed for abort times ranging from 50 to 100 seconds after launch. The corresponding payload mass delivered to orbit ranged from 64 to 74 klbm. For abort times prior to 50 seconds, the thrust to weight

ratio of the vehicle is insufficient to make the ascent to orbit.

One of the performance measures used for the RTLS maneuvers was the time of the abort. By maximizing the abort time, the window of decision for determining which abort maneuver (ATO or RTLS) to perform is maximized. For a single-engine-out scenario, maximum abort times were found for maximum attack angles varying from 60° to 90° . The corresponding abort times ranged from 130 to 183 seconds after launch. The vehicle carried the nominal payload mass of 20 klbm.

Because the vehicle has single-engine-out capability from the pad, the conclusion was made that RTLS maneuvers should only be made if the mass of the payload was larger than that which could be delivered to orbit with an ATO maneuver. This assumed that an RTLS maneuver could be made at the time of the engine failure. To check this assumption, RTLS maneuvers which maximized the payload to be returned to the launch site were studied. RTLS abort maneuvers were initiated at times ranging from 0 to 100 seconds for single-engine-out scenarios and from 50 to 100 seconds for the two-engine-out scenario. The studies showed that the maximum payload mass that can be delivered to orbit by a vehicle with a full complement of engines (80.25 klbm) could also be returned to the launch site for each of the combinations of abort times and number of engine failures examined.

To determine the entire range of payloads that could be returned to the launch site, RTLS maneuvers which minimized the payload mass to be returned to the launch site were also studied. These studies showed that the minimum payload mass was zero for each of the combinations of abort times and number of engine failures investigated.

Additional work in the area of SSTO abort performance might include optimally shaping the ascent trajectory of a healthy vehicle such that the window of decision for determining which abort maneuver ATO or RTLS to perform is maximized for range of specified payload masses to be delivered to orbit. Secondly, the numerical approach used to produce these results might be improved by incorporating a more accurate integration scheme for determining the state equation constraints.

Bibliography

- [1] National Aeronautics and Space Administration, "Access to Space Study - Summary Report", *Office of Space Systems Development, NASA Headquarters*, January 1994
- [2] Naftel, C., Englund, W., Lepsch, R., Powell, R., Bacon, J. "Ascent Abort Capability for a Rocket-Powered Single Stage Advanced Manned Launch System", AIAA 93-3694 *AIAA/Atmospheric Flight Mechanics Conference*, July, 1993
- [3] Stanley, D.O., Englund, W.C., Lepsch, R.A., McMillin, M., Wurster, K.E., Powell, R.W., Guinta, A.A., Unal, R., "Rocket-Powered Single-Stage Vehicle Configuration Selection and Design", AIAA-93-1053, *AIAA/AHS/ASEE Aerospace Design Conference*, Irvine, CA, February 1993
- [4] Huether, J.E., Spears, J.M., McCleskey, C.M., Rhodes, R.E., "Space Shuttle to Reusable Launch Vehicle", *NASA Kennedy Space Center*, March 1995
- [5] Austin, R.E., "SSTO Rockets : Streamlining Access to Space", *Aerospace America*, November 1994
- [6] Bless, R., Moerder, D., "Computationally Efficient Method for Multidimensional Data Interpolation", AIAA 95-3322, *AIAA Guidance, Navigation and Control Conference*, Baltimore, MD, August, 1995
- [7] Bryson, A.E., Ho, Y., *Applied Optimal Control - Optimization, Estimation, and Control*, Hemisphere Publishing Corporation, New York, NY, 1975

- [8] Gill, P.E., Murray, W., Saunders, M.A., Wright, M.H., "User's Guide for NPSOL (Version 4.0) : A Fortran Package for Nonlinear Programming", *Technical Report SOL 86-2*, Systems Optimization Laboratory, Department of Operations Research, Stanford University, January 1986

- [11] Hull, D.G., Speyer, J.L., "Optimal Reentry and Plane-Change Trajectories", *Journal of the Astronautical Sciences*, Vol. 30, No. 2, April-June, 1982

- [10] Meirovitch, L., *Methods of Analytical Dynamics*, McGraw-Hill Publishing Company, 1970

Appendix A

Development of 3-DOF Equations of Motion for a SSTO Vehicle

In this appendix, a Newtonian mechanics approach is used to develop the equations of motion for a rocket traveling over a rotating Earth. This development is highly influenced by [10].

A.1 Reference Frames

The reference frames used in this development are discussed in this section. The origin, fundamental plane and fundamental direction of each frame is defined. Illustrations showing how the different frames are related are included.

A.1.1 Earth-Centered Inertial Frame

The origin of the inertial frame (I-frame) is at the center of the Earth. The fundamental plane of this system is the equatorial plane. The fundamental direction is along the vector connecting the center of the Earth to the center of the Sun at vernal equinox.

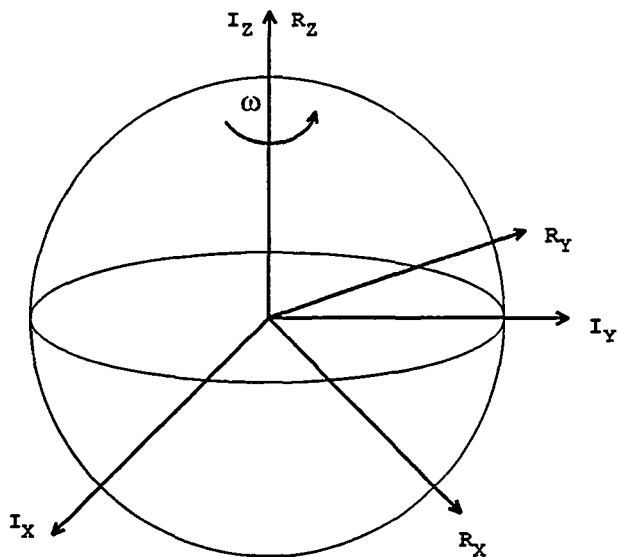


Figure A.1: I-frame and R-frame

A.1.2 Earth-Centered Rotating Frame

Like the I-frame, the origin of the rotating frame (R-frame) is at the center of the Earth. The I-frame and R-frame also share the same fundamental plane, the equatorial plane. The fundamental direction of this plane is coincident with the Greenwich Meridian at all times in the fundamental plane. Figure A.1 shows the relationship between the I-frame and the R-frame. The I_x and R_x axes are respectively the fundamental directions of the I-frame and R-frame systems. The fundamental planes are $I_x - I_y$ for the I-frame and $R_x - R_y$ for the R-frame. The R-frame rotates with angular velocity, ω (rotation rate of the Earth).

A.1.3 Position Frame

The origin of the position frame (P-frame) is at the center of mass of the SSTO vehicle. The fundamental plane is the local horizontal plane and the fundamental direction is due east. Figure A.2 illustrates the location and orientation of the P-frame relative to the R-frame. The fundamental direction of the P-frame is the P_θ axis. The fundamental plane is the $P_\theta - P_\phi$ plane. The vector, \bar{r} , is the position

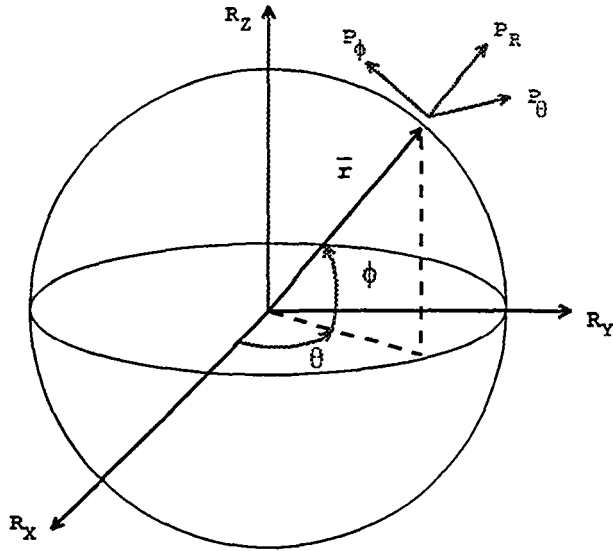


Figure A.2: R-frame and P-frame

vector of the center of mass of the SSTO vehicle.

A.1.4 Velocity Frame

The origin of the velocity frame (S-frame) is at the center of mass of the SSTO vehicle. The normal of the fundamental plane is the velocity vector relative to the R-frame. The fundamental direction is in the direction of increasing heading angle. Figure A.3 shows the relationship between the P-frame and the S-frame. The fundamental direction of the S-frame is the S_ψ axis. The fundamental plane of this frame is the $S_\psi - S_\gamma$ plane.

A.1.5 Body Frame

The origin of the body frame (B-frame) is also at the center of mass of the SSTO vehicle. The normal of the fundamental plane is the vector pointing from the center of mass to the nose of the vehicle. The fundamental direction is directed along the right wing. In figure A.4 the relationship between the S-frame and B-frame is illustrated. The fundamental direction of the B-frame is the B_y axis. The fundamental plane of

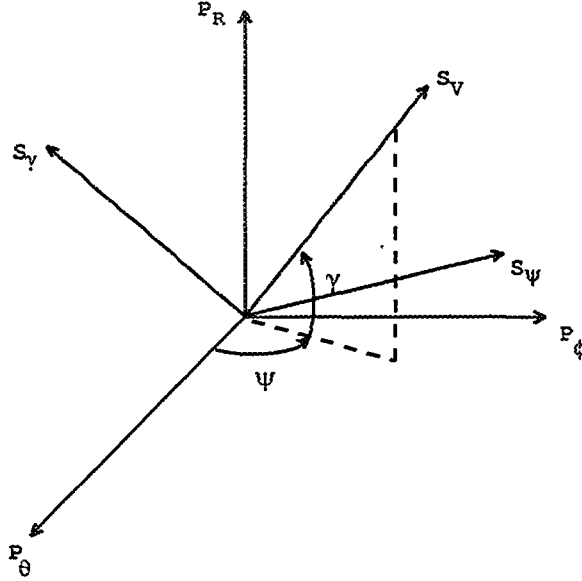


Figure A.3: P-frame and S-frame

this frame is the $B_y - B_z$ plane. The vector, \bar{T} , is the thrust vector which is directed along the longitudinal axis of the body, B_x .

A.2 Development of Equations of Motion

As shown by figure A.1 the R-frame rotates with angular velocity relative to the I-frame of

$$\bar{\omega}_{R/I} = \omega \bar{R}_z \quad (\text{A.1})$$

The angular velocity of the P-frame relative to the R-frame is

$$\bar{\omega}_{P/R} = \dot{\theta} \bar{R}_z - \dot{\phi} \bar{P}_\theta \quad (\text{A.2})$$

The \bar{R}_z unit vector expressed in terms of P-frame unit vectors is

$$\bar{R}_z = \sin \phi \bar{P}_R + \cos \phi \bar{P}_\phi \quad (\text{A.3})$$

Using relation A.3 equation A.2 becomes

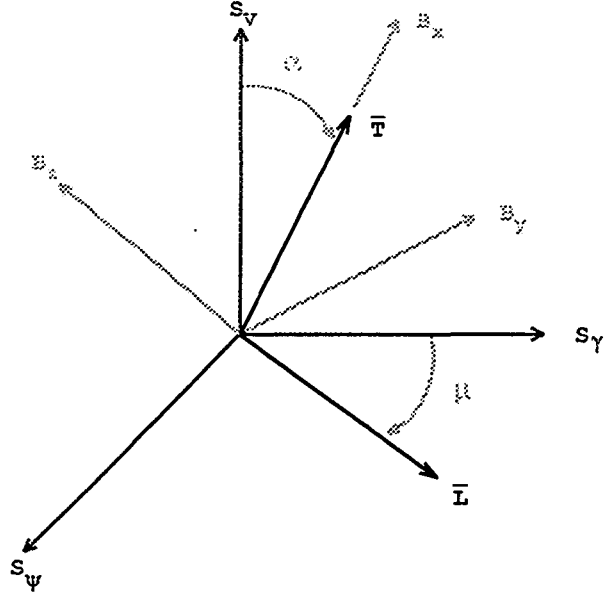


Figure A.4: S-frame and B-frame

$$\bar{\omega}_{P/R} = \dot{\theta} \sin \phi \bar{P}_R - \dot{\phi} \bar{P}_\theta + \dot{\theta} \cos \phi \bar{P}_\phi \quad (\text{A.4})$$

The angular velocity of the P-frame relative to the I-frame is found using

$$\bar{\omega}_{P/I} = \bar{\omega}_{P/R} + \bar{\omega}_{R/I} \quad (\text{A.5})$$

This expression yields

$$\bar{\omega}_{P/I} = (\dot{\theta} + \omega) \sin \phi \bar{P}_R - \dot{\phi} \bar{P}_\theta + (\dot{\theta} + \omega) \cos \phi \bar{P}_\phi \quad (\text{A.6})$$

The velocity of the Single-Stage To Orbit (SSTO) vehicle relative to the R-frame expressed in terms of P-frame unit vectors is

$$\dot{\vec{r}}_P = \dot{r} \bar{P}_R + r \dot{\theta} \cos \phi \bar{P}_\theta + r \dot{\phi} \bar{P}_\phi \quad (\text{A.7})$$

In the S-frame this velocity is expressed as

$$\dot{\vec{r}}_S = v \bar{S}_V \quad (\text{A.8})$$

The rotation matrix that rotates P-frame vectors to S-frame vectors is given by

$$\begin{bmatrix} \bar{S}_V \\ \bar{S}_\psi \\ \bar{S}_\gamma \end{bmatrix} = \begin{bmatrix} \cos \gamma \cos \psi & \cos \gamma \sin \psi & \sin \gamma \\ -\sin \psi & -\cos \psi & 0 \\ -\sin \gamma \cos \psi & -\sin \gamma \sin \psi & \cos \gamma \end{bmatrix} \begin{bmatrix} \bar{P}_\theta \\ \bar{P}_\phi \\ \bar{P}_R \end{bmatrix} \quad (\text{A.9})$$

Using the inverse of this rotation matrix equation, A.8 is expressed in terms of P-frame unit vectors

$$\dot{\bar{r}}_P = v \sin \gamma \bar{P}_R + v \cos \gamma \cos \psi \bar{P}_\theta + v \cos \gamma \sin \psi \bar{P}_\phi \quad (\text{A.10})$$

Equating expressions A.7 and A.10 yields

$$\left. \begin{aligned} \dot{\theta} &= v \cos \gamma \cos \psi / (r \cos \phi) \\ \dot{\phi} &= v \cos \gamma \sin \psi / r \\ \dot{r} &= v \sin \gamma \end{aligned} \right\} \quad (\text{A.11})$$

The angular velocity of the S-frame relative to the P-frame is

$$\bar{\omega}_{S/P} = \dot{\psi} \sin \gamma \bar{S}_V - \dot{\gamma} \bar{S}_\psi + \dot{\psi} \cos \gamma \bar{S}_\gamma \quad (\text{A.12})$$

Similar to equation A.5 the angular velocity of the S-frame relative to the I-frame is found using

$$\bar{\omega}_{S/I} = \bar{\omega}_{S/P} + \bar{\omega}_{P/I} \quad (\text{A.13})$$

Making use of expressions A.9 and A.6, equation A.13 becomes

$$\left. \begin{aligned} \bar{\omega}_{S/I} &= \dot{\psi} \sin \gamma + v/r(\cos \gamma \sin \gamma \cos \psi \tan \phi) + \omega(\cos \phi \cos \gamma \sin \psi + \sin \phi \sin \gamma) \bar{S}_V \\ &\quad - \dot{\gamma} + v \cos \gamma / r + \omega \cos \phi \cos \psi \bar{S}_\psi \\ &\quad + \dot{\psi} \cos \gamma + v/r(\cos^2 \gamma \cos \psi \tan \phi) + \omega(\sin \phi \cos \gamma - \cos \phi \sin \gamma \sin \psi) \bar{S}_\gamma \end{aligned} \right\} \quad (\text{A.14})$$

The position of the S-frame origin is

$$\bar{r}_{S_o} = r \sin \gamma \bar{S}_V + r \cos \gamma \bar{S}_\gamma \quad (\text{A.15})$$

The absolute velocity of the S-frame origin (i.e. SSTO center of mass) is found using

$$\dot{\bar{r}}_{S_o} = r_V \dot{\bar{S}}_V + r_\psi \dot{\bar{S}}_\psi + r_\gamma \dot{\bar{S}}_\gamma + \bar{\omega}_{S/I} \times \bar{r}_{S_o} \quad (\text{A.16})$$

where

r_V = Component of S-frame Origin Along \bar{S}_V

r_ψ = Component of S-frame Origin Along \bar{S}_ψ

r_γ = Component of S-frame Origin Along \bar{S}_γ

After some simplification, equation A.16 becomes

$$\begin{aligned} \dot{\bar{r}}_{S_o} = & (v + \omega r \cos \phi \cos \psi \cos \gamma) \bar{S}_V \\ & - (\omega r \cos \phi \sin \psi) \bar{S}_\psi \\ & - (\omega r \cos \phi \cos \psi \sin \gamma) \bar{S}_\gamma \end{aligned} \quad (\text{A.17})$$

Similarly, the absolute acceleration of the S-frame origin is found using

$$\ddot{\bar{r}}_{S_o} = v_V \dot{\bar{S}}_V + v_\psi \dot{\bar{S}}_\psi + v_\gamma \dot{\bar{S}}_\gamma + \bar{\omega}_{S/I} \times \dot{\bar{r}}_{S_o} \quad (\text{A.18})$$

where

v_V = Component of S-frame Origin Velocity Along \bar{S}_V

v_ψ = Component of S-frame Origin Velocity Along \bar{S}_ψ

v_γ = Component of S-frame Origin Velocity Along \bar{S}_γ

After a few pages of algebra, expression A.18 becomes

$$\begin{aligned}
\ddot{\bar{r}}_{S_0} = & [\dot{v} - \omega^2 r \cos \phi (\sin \gamma \cos \phi - \cos \gamma \sin \phi \sin \psi)] \bar{S}_V \\
& + [\dot{\psi} + \omega^2 r \sin \phi \cos \phi \cos \psi / (v \cos \gamma) - 2\omega (\tan \gamma \cos \phi \sin \psi - \sin \phi) \\
& + v \cos \gamma \cos \psi \tan \phi / r] v \cos \gamma \bar{S}_\psi \\
& + [\dot{\gamma} - \omega^2 r \cos \phi (\cos \gamma \cos \phi + \sin \gamma \sin \phi \sin \psi) / v \\
& - 2\omega \cos \phi \cos \psi - v \cos \gamma / r] v \bar{S}_\gamma
\end{aligned} \tag{A.19}$$

The forces acting on the SSTO include : Earth gravitational force, SSTO thrust, aerodynamic lift and aerodynamic drag. The resultant of these forces expressed in the S-frame is

$$\begin{aligned}
\bar{F} = & (T \cos \alpha - D - mg \sin \gamma) \bar{S}_V \\
& + (T \sin \alpha \sin \mu + L \sin \mu) \bar{S}_\psi \\
& + (T \sin \alpha \cos \mu + L \cos \mu - mg \cos \gamma) \bar{S}_\gamma
\end{aligned} \tag{A.20}$$

From Newton's second law

$$m \ddot{\bar{r}}_{S_0} = \bar{F} \tag{A.21}$$

This yields

$$\left. \begin{aligned}
\dot{v} &= (T \cos \alpha - D) / m - g \sin \gamma + \omega^2 r \cos \phi (\sin \gamma \cos \phi - \cos \gamma \sin \phi \sin \psi) \\
\dot{\psi} &= (T \sin \alpha \sin \mu + L \sin \mu) / (mv \cos \gamma) - \omega^2 r \sin \phi \cos \phi \cos \psi / (v \cos \gamma) \\
&\quad + 2\omega (\tan \gamma \cos \phi \sin \psi - \sin \phi) - v \cos \gamma \cos \psi \tan \phi / r \\
\dot{\gamma} &= (T \sin \alpha \cos \mu + L \cos \mu) / (mv) + \omega^2 r \cos \phi (\cos \gamma \cos \phi + \sin \gamma \sin \phi \sin \psi) / v \\
&\quad + 2\omega \cos \phi \cos \psi + (v / r - g / v) \cos \gamma
\end{aligned} \right\} \tag{A.22}$$

Appendix B

NLP Scheme Used To Solve Optimal Control Problems

The NLP scheme used to solve the optimal control problems in this study employs an existing optimization algorithm named NPSOL [8]. Developed at Stanford University, NPSOL is a set of Fortran subroutines designed to minimize a smooth function subject to constraints. NPSOL requires the user to supply a main or driver program and subroutines that define the objective and constraint functions and (optionally) their gradients.

A group of subroutines that compose the multi2 library are used to convert optimal control problems into a NLP problems and supply NPSOL with the required objective and constraint functions subroutines. No gradient information is supplied by these subroutines. Therefore, NPSOL must calculate all gradients numerically.

The user of this scheme supplies six subroutines and a driver routine. The six subroutines interface with the multi2 library to yield the objective and constraint functions. Figure B.1 provides an illustration of the scheme. In this figure, the arrows point to a subroutine that is called by the routine at the end of the arrow. The user supplied subroutines and driver program are capitalized and the multi2 library subroutines are represented with asterisks.

A brief description of each of the routines in this scheme is given below.

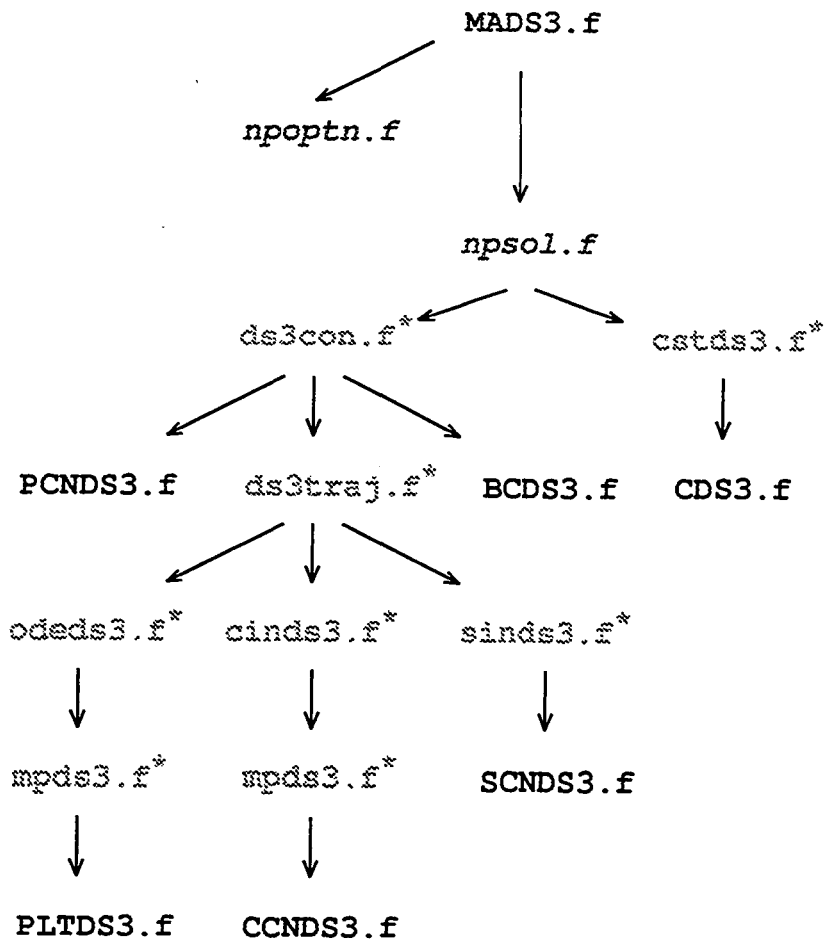


Figure B.1: NLP Scheme

User Supplied Routines

MADS3.f : Driver Program
CDS3.f : Evaluates Cost Function
BCDS3.f : Evaluates Boundary Condition Constraints
PLTDS3.f : Evaluates State Equations
CCNDS3.f : Evaluates State/Control Inequality Constraints
SCNDS3.f : Evaluates State-Only Inequality Constraints
PCNDS3.f : Evaluates Free Parameter Inequality Constraints

Multi2 Library Routines

cstds3.f : Supplies NPSOL with Objective Function Value
ds3con.f : Supplies NPSOL with Values of Constraints
ds3traj.f : Evaluates Constraints Along Trajectory
odeds3.f : Evaluates State Equation Constraints Along Trajectory
cinds3.f : Evaluates State/Control Inequality Constraints Along Trajectory
sinds3.f : Evaluates State-Only Inequality Constraints Along Trajectory
mpds3.f : Calculates Nodal Midpoints

NPSOL Routines

npoptn.f : Supplies NPSOL with Optional Input Parameters
npsol.f : Solves the NLP problem

As authored by Dr. Dan Moerder, this scheme originally had only single phase capability. The author of this study extended the capabilities of this code to handle multiple phase problems.

REPORT DOCUMENTATION PAGE			Form Approved OMB No 0704-0188	
Public reporting burden for this collection of information is estimated to average 1 hour per response, including the time for reviewing instructions, searching existing data sources, gathering and maintaining the data needed, and completing and reviewing the collection of information. Send comments regarding this burden estimate or any other aspect of this collection of information, including suggestions for reducing this burden, to Washington Headquarters Services, Directorate for Information Operations and Reports, 1215 Jefferson Davis Highway, Suite 1204, Arlington, VA 22202-4302, and to the Office of Management and Budget, Paperwork Reduction Project (0704-0188), Washington, DC 20503.				
1 AGENCY USE ONLY (Leave blank)	2. REPORT DATE August 1995	3 REPORT TYPE AND DATES COVERED Contractor Report		
4. TITLE AND SUBTITLE Abort Performance for a Winged-Body Single-Stage to Orbit Vehicle			5. FUNDING NUMBERS NCC1-104 WU 242-80-01-02	
6 AUTHOR(S) Jeffery A. Lyon				
7 PERFORMING ORGANIZATION NAME(S) AND ADDRESS(ES) The George Washington University Joint Institute for Advancement of Flight Sciences NASA Langley Research Center Hampton, VA 23681-0001			8. PERFORMING ORGANIZATION REPORT NUMBER	
9 SPONSORING / MONITORING AGENCY NAME(S) AND ADDRESS(ES) National Aeronautics and Space Administration Langley Research Center Hampton, VA 23681-0001			10 SPONSORING / MONITORING AGENCY REPORT NUMBER NASA CR-4690	
11 SUPPLEMENTARY NOTES The information presented in this report was offered as a thesis by the author in partial fulfillment of the requirements for the Degree of Master of Science, The George Washington University, July 1995 Langley Technical Monitor: Daniel D Moerder				
12a. DISTRIBUTION / AVAILABILITY STATEMENT Unclassified - Unlimited Subject Category 15			12b DISTRIBUTION CODE	
13 ABSTRACT (Maximum 200 words) Optimal control theory is employed to determine the performance of abort to orbit (ATO) and return to launch site (RTL) maneuvers for a single-stage to orbit vehicle. The vehicle configuration examined is a seven engine, winged-body vehicle, that lifts-off vertically and lands horizontally. The abort maneuvers occur as the vehicle ascends to orbit and are initiated when the vehicle suffers an engine failure. The optimal control problems are numerically solved in discretized form via a non-linear programming (NLP) algorithm. A description highlighting the attributes of this NLP method is provided. ATO maneuver results show that the vehicle is capable of ascending to orbit with a single engine failure at lift-off. Two engine out ATO maneuvers are not possible from the launch pad, but are possible after launch when the thrust to weight ratio becomes sufficiently large. Results show that single engine out RTL maneuvers can be made for up to 180 seconds after lift-off and that there are scenarios for which RTL maneuvers should be performed instead of ATP maneuvers.				
14 SUBJECT TERMS Optimal Guidance, Launch Vehicles, Space Transportation, Abort Performance			15 NUMBER OF PAGES 83	
			16 PRICE CODE A05	
17 SECURITY CLASSIFICATION OF REPORT Unclassified	18. SECURITY CLASSIFICATION OF THIS PAGE Unclassified	19 SECURITY CLASSIFICATION OF ABSTRACT	20 LIMITATION OF ABSTRACT	